NTNU

Norwegian University of
Science and Technology

Ultrafast Spectroscopic Studies of Ferroelectric $BaTiO_3$ Thin-Films on $SrTiO_3$

Øystein Johannes Bergsagel

Master of Science in Electronics
Submission date: June 2016
Supervisor: Ulf Lennart Østerberg, IET
Co-supervisor: Thomas Tybell, IET

Norwegian University of Science and Technology
Department of Electronics and Telecommunications

Preface

The work for this master's thesis has been carried out at the ultrafast optics laboratory at NTNU the spring of 2016. It has been an inspiring journey, both embarking on the world of ultrafast lasers and oxide electronics. I would like thank my supervisors Prof. Thomas Tybell and Prof. Ulf Österberg. Thomas for his inspiring scientific enthusiasm and for explaining concepts of oxide electronics. I want to give a special thanks to Ulf for the guidance and good discussions, for being a great mentor, as well as making sure a steady flow of coffee got brought to the lab when checking the current status or while giving helpful advices. Additionally I would like to thank the postdoc in the lab Reza Zamiri for teaching various topics and the many discussions, as well as tips and tricks for doing experimental optics, it has been great. I want to thank Torstein Bolstad for making all the samples, as well as Prof. Ursula Gibson for letting me use her lab for sample-polishing. In addition to my classmates, friends and family who I have spent these years together with, making them memorable.

Abstract

In this masters thesis ultrafast spectroscopic studies have been performed on single-crystal <111> strontium titanate, $SrTiO_3$, and pulsed-laser deposited (PLD) thin-films of ferroelectric barium titante, $BaTiO_3$. This has been achieved by means of optical Kerr effect spectroscopy (OKE) and terahertz time-domain spectroscopy (THz-TDS). Measurements of $SrTiO_3$ in transmission geometry by THz-TDS, using THz-pulses consisting of a typical frequency band of 0.2-6 THz, resulted in very weak detectable signals, which resulted in the need for a systematic study to determine the various contributing factors to signal loss. It has been found that the low transmission of the terahertz pulse in the $500\mu m$ thick $SrTiO_3$ probably is due to high absorption or reflection by the sample, possibly due to the reported phonon modes lying in this spectral region. This showed that using $SrTiO_3$ as a substrate material did not enable any reliable measurements for the $BaTiO_3$ thin-films, implying a need for another use of THz-TDS to enable observations of absorption bands in STO and BTO. A series of measurements using the optical Kerr effect spectroscopy have been performed on various samples giving promising results. The measured OKE signals of STO and BTO provided interesting information regarding the relaxational dynamics of the system and unexpected observations in the time-domain signals motivates further study of both $SrTiO_3$ and $BaTiO_3$ using this spectroscopic method. To enable comparisons with other studies acetone has been analysed. From the measured OKE transient, the Raman spectra have been retrieved. For the OKE measurements of <111> $SrTiO_3$ samples a clear peak can be seen in a region which suggests this to be an observation of the transverse-optic TO1 phonon mode. Measurements of $BaTiO_3$ thin-films in OKE shows promising peaks which could be caused by a combination mode of the known E and A_1 phonon modes which can be found in $BaTiO_3$. As the post-processing of the measured OKE signal which is needed enable extraction of the Raman spectrum was found to be greatly affected by various parameters, further studies would need to be performed in order to determine exact positions, and confirm the physical nature of these measurements

Sammendrag

I denne masteroppgaven har ultra raske spektroskopiske metoder blitt brukt for å undersøke monokrystallinsk <111> strontium titanat, $SrTiO_3$ og tynn-filmer av ferroelektrisk barium titante, $BaTiO_3$ deponert ved hjelp av pulsert-laser deponering (PLD). Dette har blitt implementert ved å bruke de to metodene optisk Kerr effekt spektroskopi (OKE), og terahertz tids-domene spektroskopi (THz-TDS). Transmisjonsmålinger av $SrTiO_3$ for THz-TDS, hvor hver puls består av frekvens-spekteret 0.2-6 THz, resulterte i målinger av svake transmitterte signaler. Dette gjorde det nødvendig med en systematisk studie for å utelukke at eksperimentelle feilkilder var hovedårsaken til denne observasjonen, i tillegg til å se etter dominerende bidrag. Det viste seg av den lave transmisjonen trolig er forårsaket av høy absorpsjon eller refleksjon i den $500\mu m$ tykke $SrTiO_3$ prøven, som trolig kan skyldes tilstedeværælsen av de Raman-aktive rapporterte fonon-modene som finnes i denne frekvensregionen. Dette viste at å bruke $SrTiO_3$ som substrat for målinger av tynn-film $BaTiO_3$ ikke førte til noen anvendbare resultater, og at et annet oppsett eller modifikasjon for prøver er nødvendig for å muliggjøre observasjoner av absorpsjonbåndene i $BaTiO_3$ tynn-filmer. En rekke tester ved å bruke optiske Kerr effekt spektroskopi har blitt gjennomført på ulike materialer, og har vist lovende resultater. De målte OKE signalene for STO og BTO har vist en rekke interessante funn og disse uventede observasjonene som har vist seg ved ulike tids-forsinkelser fordrer til videre studier. Aceton har i tillegg blitt analysert ved hjelp av OKE for å se om de observerte resultatene samsvarer med publiserte studier. I tillegg til studier av hvordan de ulike materialene relakserer, så har også de tilsvarende Raman spektrumene blitt kalkulert. For OKE målingene av <111> $SrTiO_3$ prøvene så har det blitt observert en tydelig maksima i Raman-spektrumet som tilsier at dette er en observasjon av den transvers-optiske TO1 fonon-moden. Målinger på $BaTiO_3$ tynn-filmer i OKE har vist lovende målinger, hvor det tilsvarende Raman-spektrumet har maksima i et frekvens-område som tilsier at muligens observasjoner av en kombinasjons-mode av E and A_1 fonon modene i BTO har blitt gjort. Siden post-prosesseringen av det målte OKE signalet som muliggjør denne ekstraksjonen av Raman spektrumet viste seg å være veldig avhengig av valg av parametre, så vil videre studier være ønskelig for å kunne si eksakt posisjon, og for å bekrefte den fysiske opprinnelsen for disse målte observasjonene.

Contents

List of Figures

List of Tables

Abbreviations:

BBO β-barium borate

BS Beam-splitter

BTO Barium Titanate

DFG Difference Frequency Generation

DFT Discrete Fourier Transform

EEPROM Electrically Erasable Programmable Read-only Memory

EO Electro-optic

FET Field-effect transistor

FFT Fast Fourier transform

FRAM Ferroelectric random access memory

FWHM Full width at half maximum

FWM Four wave mixing

IR Infrared

ITO Indium tin oxide

MRAM Magnetic random access memory

NLO Nonlinear optics

OKE Optical Kerr Effect Spectroscopy

PCA Photoconductive antenna

PLD Pulsed laser deposition

PSD Phase-sensitive Detector

QWP Quarter-wave plate

RMS Root mean square

RSD Reduced spectral density

SFG Sum Frequency Generation

SHG Second Harmonic Generation

STO Strontium Titanate

SRS Stimulated Raman scattering

THz-TDS Terahertz time domain spectroscopy

US Ultrasonic

Chapter 1

Introduction

Background and Motivation

When Shockley, Bardeen and Brattain built the transistor at Bell labs in 1947, later earning them a Nobel Prize in physics [1], it marked the beginning of a new era of electronics. Going from bulky and low density analogue devices to miniaturization and digitalization. Phenomena and concepts which previously had only been seen as theoretical possibilities were gradually being discovered and utilized in real life. Be it quantum-phenomena proposed in the early 1900s by Einstein and Planch, by the invention of the laser in the early 60s, using the concept of stimulated emission, or the invention of electrically-erasable programmable read-only memory (EEPROM) in the late 70s using quantum-tunneling. The scientific discoveries and technological development over the last 60 years has been enormous, and it would take more than one master thesis to briefly mention even just a fraction of these. However, one aspect which has become of paramount importance in a vast variety of technological fields and still is advancing its position is the materials science. If we limit the scope to the electronics industry none of the current technology we see today would be possible without a sound knowledge of material physics; effect of doping, electronic transport properties, heat transport, structural stability, interface effects, it has all come to play an important part. For the semiconductor industry the well known Moore's law has been a benchmark when it comes to capacity increase as it predicted a 100% increase in density of components for integrated circuits every two years since the 60s [2]. In recent years, especially after 2010 due to physical limitations and power constraints there has been an increasing interest in what is known as more-than-Moore [3], where the focus has been shifted from increased performance to additional features. For the sake of this new focus there has been increased efforts in researching materials that show interesting properties that might be exploited for such a cause. One specific example of such a system which would require very low power consumption and limited processing power are sensors for infrastructure and buildings. The ability to look at strain and changes

in inaccessible parts of buildings would enable real-time monitoring of structural integrity and thereby also better safety. Such systems would not require much processing power, but be a more-than-Moore focused product where additional features such as low power consumption would be crucial. One group of materials which exhibit many properties that could be useful for more-than-Moore technology are the perovskites. Study of various perovskites such as $SrTiO_3$ was performed even in the 60s [4]-[6], and has seen continuous development since as early as the 40s [7]. The reason why particularly perovskites are of interest is due to their various piezo- and pyroelectric, ferroelectric and ferromagnetic properties. Lead zirconate titanate, $Pb[Zr_xTi_{1-x}]O_3$ (PZT) is often mentioned when speaking about perovskites, since this has been extensively used as an acoustic sensor for cheap microphones due to its piezoelectric properties, applied pressure causing built up voltage across the crystal. As for ferroelectrics there are numerous applications of interest, ranging from microwave tunable filters, varactors to ferroelectric RAM [8]. An area of particular interest is also the relationship between the thin-film and bulk properties of these ferroelectrics [9]. Some of the limitation of conventional work-memory in computers are that they are mostly volatile, meaning that the information will be lost if power is turned off. Therefore there has been an interest in other technologies for random-access-memory (RAM) which is non-volatile, that still exhibit a decent transition/update speed. One developed principle is using a ferroelectric material for storage of information as polarization in material, commonly known as ferroelectric-RAM (FRAM). There exists commercial FRAM products which are low density but very long information lifetime expectancy as described in one of the early papers by Scott et al. [10]. Additionally technology using the ferromagnetic properties, magnetic RAM (MRAM) are being researched [11]. It has also been an interest in using a combination of these ferroelectric, and ferromagnetic materials for creating materials that may draw the advantages from the ferroelectric and ferromagnetic, this group is often called multiferroics. Since very few materials exhibit both these effects at the same time, multiple layers are often being used, and coupling between these layers is an important area of current research [12].

In this project the ultrafast dynamics of ferroelectric thin-films will be studied by using a set of ultrafast spectroscopic techniques. The main research goal is to be able to measure the phonon-modes in the ferroelectric barium titanate thin-film, $BaTiO_3$ on a <111> $SrTi0_3$ substrate. By using the frequency spectrum obtained from these spectroscopic techniques the phonon modes hopefully may be distinguished. Certain modes will be particularly interesting due to their direct relationship to ferroelectric properties of the material. To be able to distinguish these phonon modes would be the overall goal of this study.

There has been research groups that were able to measure phonon modes in BTO [13], [14] by using THz-TDS, but these have used MgO substrate. If this study yielded a decent result in THz-TDS with BTO on STO it would most likely be

the first study to have done so. OKE studies of BTO or STO have not yet been performed by other research groups to the best knowledge of the author, which would make this project the first. From a researchers point of view, in addition to the purely scientific interest in observing the phonon modes and studying the ultrafast dynamics, it could additionally be of great interest for thin-film development. As measurement of the phonon frequency could be used for determining trends caused by variation in fabrication parameters. Softening or hardening of the phonon-mode related to the ferroelectricity of the material would be of vital importance. The ultrafast dynamics of the atoms, and the nonlinear constants of the material would be measurable in the OKE and be of interest for further study.

The methods which will be used are the terahertz time-domain spectroscopy (THz-TDS) and optical Kerr-effect spectroscopy (OKE), both will be performed by using a high-power femtosecond laser source. The material that will be tested is a barium titanate $BaTiO_3$ (BTO) thin-film in the range of 10-100nm deposited on top of a 500μm thick <111> oriented strontium titanate $SrTiO_3$ (STO) substrate. By using the absorption peaks in the THz-TDS, or corresponding peaks in the Raman spectrum for OKE, combined with appropriate models hopefully the presence and frequency of the phonon modes will be determined. As a result of these measurements being performed at room temperature it is likely that broad phonon-resonances will be seen and possibly combination modes, so analysing the data and using the appropriate models will be crucial for a good understanding of the phenomena occurring. If phonon modes are distinguishable and if time allows looking at the response along different crystalline axes will also be performed.

Outline

The structure of this thesis will be as follows: After this introduction a theory section will follow. This part will go through the most important concepts which should provide the reader with a short but concise explanation of the different phenomena and theories relevant for the work in this masters thesis. For a more in-depth study of these individual concepts please refer to the supporting literature. This will be followed by the experimental sections, where the schematics and operating principles for both the OKE and THz-TDS will be more thoroughly explained. Accompanied by sample and data preparation, analysis and results. The section following will be the discussion where results will be further examined and experimental observations will be deliberated. The last section with concluding remarks and a short summary of the results, in addition to suggestions for future work will be the conclusion.

Chapter 2

Background Material and Theory

2.1 Optics

Before the development of quantum-mechanics, light was described classically, either as rays or waves. The ray picture made for the development of geometrical optics, which was later followed by the wave-description of light. This enabled explanations of many optical effects, such as interference, refraction and diffraction. The theory which makes for the foundation of describing electro-magnetic waves was developed by James Clerk Maxwell in the 1800s:

$$\begin{aligned} \nabla \times \mathbf{H} &= \frac{\partial \mathbf{D}}{\partial t} + \sigma J, \qquad & \nabla \cdot \mathbf{D} &= -\rho_V, \\ \nabla \times \mathbf{E} &= -\frac{\partial \mathbf{B}}{\partial t}, & \nabla \cdot \mathbf{B} &= 0, \end{aligned} \tag{2.1}$$

However with the discovery of the photoelectric effect by Einstein early 1900s, classical physics could no longer be used to explain the occurring phenomena, and the quantum-description of light was developed. The particle-nature of light enabled new phenomena to be explained, describing light by their energy quanta, namely the photon: $E_{photon} = h\nu$. These two descriptions of electro-magnetic waves will be interchangeably used in the following sections.

2.1.1 Light-matter interaction

The propagation of light through a material is characterized by the complex refractive index $\tilde{n} = n + i\kappa$. The linear refractive index n is material dependent and describes the phase-velocity v of the EM-wave as it propagates through a medium relative to the light velocity in vacuum c_0, $v = c_0/n$. The extinction coefficient κ is directly related to absorption α by $\kappa = \frac{\alpha\lambda}{4\pi}$, where λ is the wavelength. A common notation which is also used to describe the material properties is using the complex dielectric constant $\tilde{\epsilon_r} = \epsilon_1 + i\epsilon_2$ which is related to the complex refractive index by:

$$\tilde{n} = \sqrt{\epsilon_r} \implies \tilde{n}^2 = \epsilon_r \tag{2.2}$$

Consequently the linear refractive index and the absorption coefficient can both be found from the complex dielectric constant. For most materials the light velocity and absorption will in addition be dependent on frequency, $\tilde{n}(\nu)$, such materials are called dispersive.

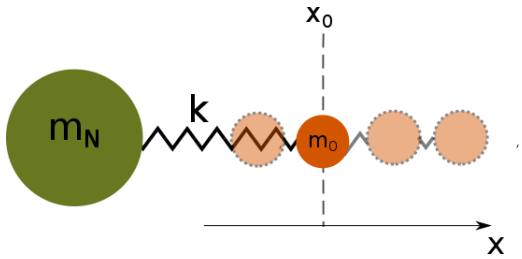

Figure 2.1: Dipole Oscillator

A common way to describe light-matter interaction is to look at it as atomic dipoles, a negative electron bound by a spring to the centre of the atom, the nucleus. The natural frequency is given as

$$\omega_0 = \sqrt{\frac{K_S}{\mu}} \tag{2.3}$$

where μ is the so-called reduced mass, described by the electron mass m_0 and mass of the nucleus m_N : $\frac{1}{\mu} = \frac{1}{m_0} + \frac{1}{m_N}$. An incoming wave would act as a force upon the electron and nucleus, leading to a displacement proportional to the spring constant and thus be proportional to the dipole moment. Since the mass of the nucleus is significantly larger than the electron mass, the motion of the nucleus can be approximated to zero, this gives the corresponding electron-displacement:

$$m_0 \frac{d^2x}{dt^2} + m_0\gamma\frac{dx}{dt} + m_0\omega_0^2 x = -e\mathcal{E} \tag{2.4}$$

The result is the real and imaginary parts of the dielectric function:

$$\epsilon_1(\omega) = 1 + \chi + \frac{Ne^2}{\epsilon_0 m_0}\frac{\omega_0^2 - \omega^2}{(\omega_0^2 - \omega^2)^2 + (\gamma\omega)^2} \tag{2.5}$$

$$\epsilon_2(\omega) = \frac{Ne^2}{\epsilon_0 m_0}\frac{\gamma\omega}{(\omega_0^2 - \omega^2)^2 + (\gamma\omega)^2} \tag{2.6}$$

where it is common to simplify equation 2.5 and 2.6 by using the high and low frequency limits, $\epsilon_r(0) \equiv \epsilon_{st}$ and $\epsilon_r(\infty) \equiv \epsilon_\infty$.
The relationship between the complex dielectric permittivity $\tilde{\epsilon} = \epsilon_1 + i\epsilon_2$ and the complex refractive index $\tilde{n} = n + i\kappa$ is given by:

$$n = \frac{1}{\sqrt{2}} \left(\epsilon_1 + (\epsilon_1^2 + \epsilon_2^2)^{1/2} \right)^{1/2} \tag{2.7}$$

$$\kappa = \frac{1}{\sqrt{2}} \left(-\epsilon_1 + (\epsilon_1^2 + \epsilon_2^2)^{1/2} \right)^{1/2} \tag{2.8}$$

For a more detailed derivation please refer to Fox [15].

2.1.2 Nonlinear Optics

With the invention of the laser, another group of phenomena became important and measurable, namely the nonlinear optical effects. It was discovered that at high intensities materials might cause new and interesting effects on the interacting EM-waves. The origin of these effects can be found by looking at the general definitions for EM-waves. The electric displacement field is defined as:

$$\mathbf{D} = \epsilon_0 \mathbf{E} + \mathbf{P} = \epsilon_0 (1 + \chi) \mathbf{E} = \epsilon_0 \epsilon_r \mathbf{E} \tag{2.9}$$

With the polarization given as:

$$\mathbf{P} = \epsilon_r \mathbf{E} = \epsilon_0 \chi \mathbf{E} \tag{2.10}$$

In the regime of linear optics, which is assumed when using traditional low-intensity sources the polarization is linearly dependent on the electric field:

$$\mathbf{P} = \epsilon_0 \chi^{(1)} \mathbf{E} \tag{2.11}$$

where the refractive index is given as:

$$n = \sqrt{\epsilon_r} = \sqrt{1 + \chi^{(1)}} \tag{2.12}$$

However, if the light-intensity is sufficiently high the nonlinear effects needs to be taken into consideration. Compared to linear optics the nonlinear regime provides new possibilities by using a new set of optical phenomena. It was discovered that in this new regime the resulting polarization caused by an incident electric field could also show properties contributed by the square and cube of the electric field.

$$\mathbf{P} = \epsilon_0 (\chi^{(1)} \mathbf{E} + \chi^{(2)} \mathbf{E}^2 + \chi^{(3)} \mathbf{E}^3 + \cdots) \tag{2.13}$$

In the regime of linear optics, one assumes that intensity is low so that the nonlinear effects will not be present, therefore only $\chi^{(1)}$ is needed for calculation of the displacement-field, and will be sufficient to describe the propagating wave.

2nd Order Nonlinearities

A nonlinear optical effect is commonly classified by whether it depends on $\mathbf{E}^2$ or $\mathbf{E}^3$, corresponding in a second- or third-order nonlinearity respectively. Whether a second- or third-order nonlinear optical (NLO) effect will be present depends on the material properties and phase-matching of the interacting waves. Generally centro-symmetric materials will not exhibit second-order nonlinearities due to inversion symmetry [17]. By insertion of a simple plane wave in the expression for the polarization these new phenomena can be shown mathematically. The second order nonlinear effects resulting from a set of monochromatic beams can be explained in the following manner. Not taking into consideration any spatial variations, only as a function of time, these may be described as:

$$\mathbf{E} = A\cos(\omega t) \tag{2.14}$$

This would result in the polarization:

$$\begin{aligned}\mathbf{P} = \epsilon_0(\chi^{(1)}\mathbf{E} + \chi^{(2)}\mathbf{E}^2) &= \epsilon_0(\chi^{(1)}A\cos(\omega t) + \chi^{(2)}(A\cos(\omega t))^2) \\ &= \epsilon_0(\chi^{(1)}A\cos(\omega t) + \frac{1}{2}\chi^{(2)}A^2(1+\cos(2\omega t))\end{aligned} \tag{2.15}$$

These two terms can be divided into the linear and nonlinear contribution respectively. For the nonlinear term it can be seen that it now appears a constant invariant of time:

$$\mathbf{P}_{NL} = \epsilon_0\frac{1}{2}\chi^{(2)}A^2 + \epsilon_0\frac{1}{2}\chi^{(2)}A^2\cos(2\omega t)$$

this is called optical rectification. In addition to a time-varying contribution having twice the frequency of the original wave namely the second harmonic, causing second-harmonic generation (SHG). Shown below is a list of second order nonlinear effects which are dependent on the $\chi^{(2)}$ of the material:

Optical rectification: The incoming wave induces a static polarization in the material.

Second-harmonic generation (SHG): Part of the incoming field will be frequency doubled, meaning that if one were to send in $\lambda = 800nm$ a portion would be transformed into light with $\lambda = 400nm$.

Sum-frequency generation (SFG): Two incident waves on a material with different wavelengths will have some of their energy transferred into a third wave having frequency equal to the sum of the two incoming waves.

Difference-frequency generation (DFG): Similar to SFG, but the generated wave will have frequency equal to the difference between the two waves.

Pockels effect: If a static field is applied, meaning that the interacting wave would be of the form: $\mathbf{E} = A_0 + A_1\cos(\omega t)$, the Pockels effect might be observed. This nonlinear phenomenon causes the refractive index to be linearly

dependent on the applied static field:

$$n = \sqrt{\epsilon} = \sqrt{1 + \chi^{(1)} + 2\chi^{(2)} A_0} \tag{2.16}$$

where A_0 is the amplitude of the static field. Due to this linear relationship the Pockels effect is used in many optical applications, such as interferometric techniques; having two co-propagating paths, one being controlled with a Pockels cell, by changing the refractive index one could thereby change the relative phase, thereby have the paths interfere constructively or destructively.

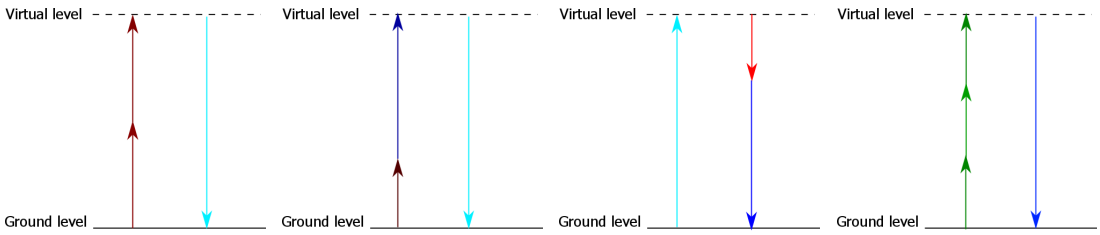

(a) SHG (b) SFG (c) DFG (d) THG

Figure 2.2: Second order nonlinear optical phenomena

3rd Order Nonlinearities

For the third-order nonlinear susceptibility $\chi^{(3)}$ another set of optical phenomena can be present. One of them is of great importance for the experimental parts of this thesis, namely the Optical Kerr Effect.
It should be noted that for third-order nonlinearities it also exists the DC-Kerr effect in addition to the sometimes called AC Kerr-effect or optical Kerr effect. The DC-Kerr effect can occur when a static voltage is applied to the interacting EM-waves, corresponding to waves having the form $\mathbf{E} = A_0 + A_1 \cos(\omega t)$, similarly to the requirement for obtaining the 2nd order NLO Pockels effect.

Optical Kerr-effect: The optical Kerr effect is a third-order nonlinear effect, which implies it being dependent on the interaction of three electro-magnetic waves. The phenomena causes a refraction index change in the material which is proportional to the intensity of the electric field $\mathbf{I} \propto \mathbf{E}^2$ as will be shown below.

The origin of the optical Kerr effect can be explained using a similar method as for the second-order NLO phenomena, by looking at the resulting polarization caused by interacting waves. If one assumes the simplest case of three waves having the same frequency and amplitudes interacting, and assume that the second order susceptibility is negligible which is true for most cases when $\chi^{(3)}$ is

dominant. Below it is assumed no DC field, thus the wave can be described as: $\mathbf{E} = A\cos(\omega t)$, resulting in the polarization:

$$\begin{aligned}\mathbf{P} =& \epsilon_0(\chi^{(1)}\mathbf{E} + \chi^{(3)}\mathbf{E}^3) \\ &= \epsilon_0(\chi^{(1)}A\cos(\omega t) + \frac{\chi^{(3)}}{4}(3A^3\cos(\omega t) + A^3\cos(3\omega t))\end{aligned} \tag{2.17}$$

This can be separated into the linear and nonlinear contributions to the total polarization:

$$\mathbf{P}_{NL} = \frac{\epsilon_0\chi^{(3)}}{4}3A^3\cos(\omega t) + \frac{\epsilon_0\chi^{(3)}}{4}A^3\cos(3\omega t) \tag{2.18}$$

The $\cos(3\omega t)$ leads to third-harmonic generation (THG) as shown in Fig.2.2d. When rewriting equation 2.17 and neglecting the term for THG, it becomes apparent that another term is now contributing to the refractive index:

$$\mathbf{P} = \epsilon_0\left(\chi^{(1)} + \frac{\chi^{(3)}}{4}3A^2\right)A\cos(\omega t) \tag{2.19}$$

when comparing this with equation 2.12 it gives the contribution to the refractive index Δn coming from the optical Kerr effect.

$$n = n_0 + \Delta n = n_0 + n_2 I \tag{2.20}$$

This change in refractive index is given as:

$$\Delta n = \left(\frac{3\chi^{(3)}}{4c\epsilon_0 n^2}I\right) \tag{2.21}$$

Because susceptibility is a tensor the polarization directions of the interacting waves needs to be taken into account to determine the corresponding Δn. In general the third order nonlinear polarization is given as:

$$P_i^{(3)}(\omega_4) = \epsilon_0\chi_{ijkl}^{(3)}E_j(\omega_3)E_k(\omega_2)E_l(\omega_1) \tag{2.22}$$

where $\chi_{ijkl}^{(3)}$ is a third rank tensor, thus consisting of 81 elements. For isotropic materials this can be simplified to four groups. [16]

$$\chi_{1111}^{(3)} = \chi_{1122}^{(3)} + \chi_{1221}^{(3)} + \chi_{1212}^{(3)} \tag{2.23}$$

The idea of the tensor notation is to describe how a material affects EM-waves depending on the directionality and polarizations of these waves relative to the direction dependent properties of the material itself. In general if for illustrative purposes the third-order susceptibility is set to $\chi_{1234}^{(3)}$ then the first index, 1 would correspond to the direction of the polarization for the output wave. 2,3 and 4

would in general be the polarization directions of the three incoming waves which interact. In Cartesian coordinates the subscripts would be related to either one of the x,y or z directions.

For the optical Kerr effect it can be shown that for obtaining an intensity dependent refractive index the relationship between the frequencies must be:

$$\omega_4 = \omega_2 - \omega_2 + \omega_4 \tag{2.24}$$

2.1.3 Raman Spectrum

Raman Spectroscopy - Spontaneous Raman Scattering

The main interest in the Raman spectrum which can be obtained using Raman spectroscopy is the ability to measure various energy levels of atoms and molecules, states typically corresponding to vibrational, rotational or librational motion. For solids, due to the constrained freedom of movement for the atoms, vibrational levels are the most relevant. Compared with traditional spectroscopic techniques based on absorption, Raman spectroscopy may enable extraction of material properties not otherwise obtainable. While absorption measurements using conventional light-sources can be used to look at effects such as interband electronic transitions which can provide information on the available electronic energy-levels, Raman spectroscopy detects frequency shifts and can use this to determine intraband energy states. Raman spectroscopy uses a monochromatic lightsource, a criteria is that the wavelength is far from resonance for the measured material (photon energies do not correspond to difference between electronic energy levels). This wave excites the atom or molecule to a virtual energy level, which has a very short lifetime. This in turn relaxes by spontaneous Raman scattering to either one of the lower energy levels, typically vibrational levels are most easily measured. Due to this being a spontaneous scattering process, the light is scattered at random directions, this is in turn detected by some measurement setup. This lack of directionality of the scattered photons makes for the need of very sensitive detectors, such as a photomultiplier tube (PMT). As only a small portion of the light is scattered this makes for some of the limitations of traditional Raman spectroscopy. The scattering process is called spontaneous Raman scattering and is illustrated in figure 2.3, as only one photon is needed for the interaction to occur it can be classified as a linear optical phenomena.

Stimulated Raman Scattering

Another phenomena that is used for spectroscopic measurements is the stimulated Raman scattering (SRS). For this to occur three waves are needed, which makes it a nonlinear optical phenomena. The first photon excites the electron to a virtual energy level, this is followed by the second photon which relaxes the electron to the lower energy state by means of stimulated emission. The third photon excites the electron yet again to the virtual energy level, before it relaxes by spontaneous emission. Due to the lifetime of the virtual energy level

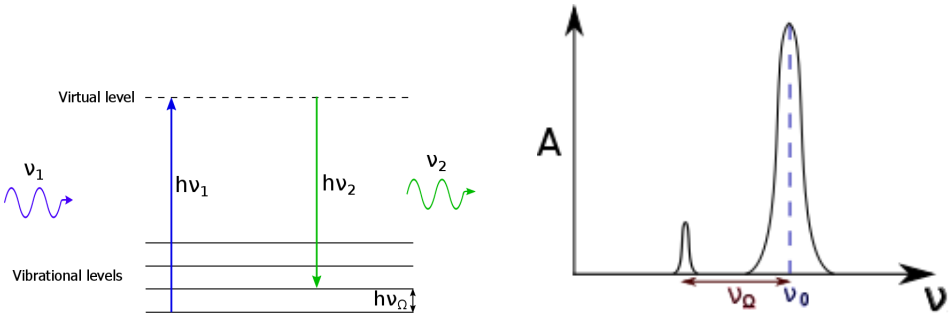

(a) Spontaneous Raman scattering (b) Stokes shifted Raman scattering

Figure 2.3: Traditional Raman Spectroscopy

being extremely short there needs to be a large amount of photons available for this phenomena to occur, which corresponds well with it being a nonlinear optical phenomena. At first glance it might seem logical that the last relaxation also contributes to the signal, however it is not likely to contribute significantly since this is a spontaeous emission process the directionality is lost, causing the photon to be scattered in any direction. One aspect which is an important factor for the significant increase in sensitivity is the stimulated emission, as this gives two photons in phase, with same frequency and same direction, in contrast to the random scattered light of spontaneous Raman scattering.

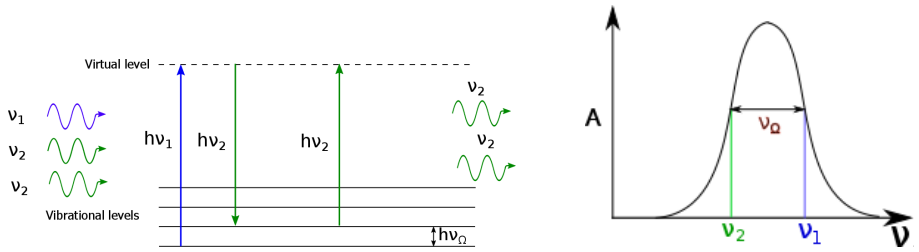

(a) Stimulated Raman (b) Stimulated Raman pulse

Figure 2.4: Stimulated Raman

Due to the fact that Raman spectrum obtained from experiments might not solely be attributed to one material property by itself but rather a combination, the resulting spectrum often needs to be decomposed by using a variety of lineshapes, corresponding to the different contributions. An example of such is shown in figure 2.5 for Ionene from the paper by Palombo et al. where contributions are reported to be corresponding with various bending and stretching modes [18].

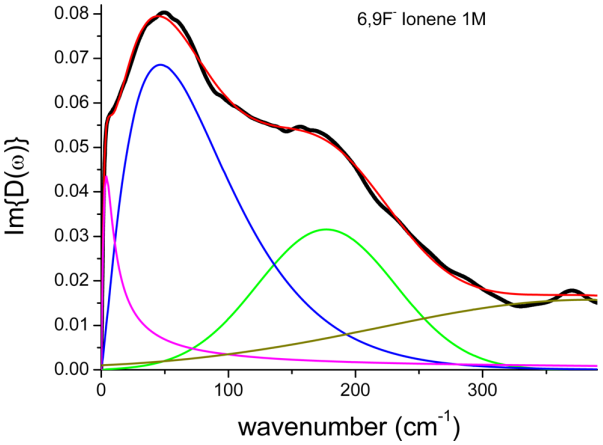

Figure 2.5: From the article by Palombo et al [18]: " Im $D(\omega)$ for 1 M 6,9 F^- ionene fit to the four line shape function: Laurentzian (Magneta), Ohmic (eq 3, blue), ASG (eq 4, green), and Gaussian (olive). The fit is shown in red."

2.1.4 Generation and Detection of Terahertz Waves

The terahertz regime was for a long time relatively inaccessible due to lack of good sources and detectors. As wavelengths corresponding to thermal heating can be found in this region the principle of conventional photodiodes would not be of much use due to massive environmental noise. With the development of the femtosecond laser new methods became available, and it was discovered that one could use these lasers to generate continuous and pulsed terahertz waves, which in turn enabled new spectroscopic techniques. A couple of detection and generation principles for THz-pulses will be described below.

Photoconductive Antenna

The photoconductive antenna (PCA), as shown in fig. 2.6, can be used both as a terahertz source and detector. The principle of a PCA emitter is to use a laser source to generate electric dipoles inside a material, which in turn causes the emission of terahertz waves. As can be seen from figure 2.6 a PCA emitter typically uses two electrodes having a static voltage applied across. The material used as a substrate typically has a very short carrier lifetime and additionally often contributes as a lens for the THz-waves. Some examples of common materials used are radiation damaged silicon on saphire (RD SOS) and low-temperature grown gallium arsenide (LT-GaAs) [19]. The incoming fs-pulse excites electron-hole pairs in the region between the electrodes. These cause a varied current density, and from Maxwells equations it can be shown that this will in turn be source for generation of an electro-magnetic field, which in this case will be the desired terahertz pulse. The shape of the generated THz-pulse

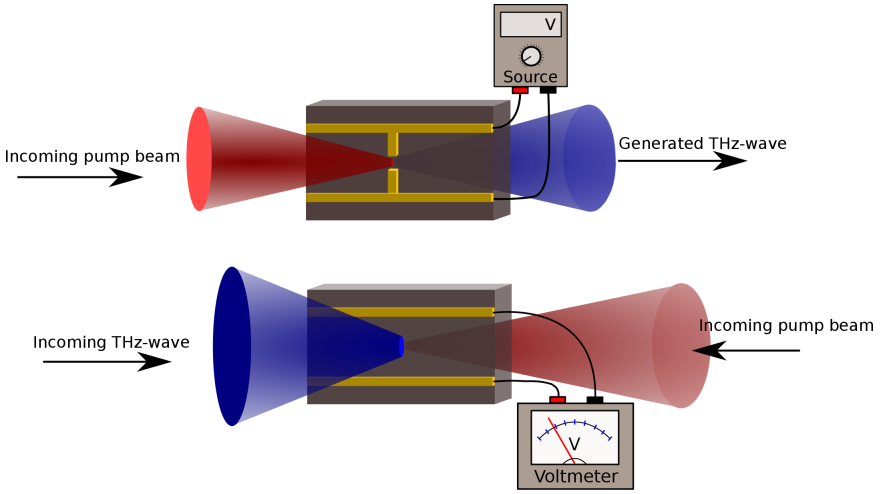

Figure 2.6: Top figure shows a photoconductive antenna THz-emitter, bottom a PCA THz-sensor. The gold-coloured lines are conductors, on top of a photoconductive substrate. An additional feature of the substrate is often making it contribute as a lens.

can be described in terms of the time evolution of the current [20]:

$$E_{THz}(t) \propto \frac{dj(t)}{dt} \tag{2.25}$$

When using a photoconductive antenna as a detector the configuration is slightly different. Still a femtosecond pulse is needed, but this time it will hit the back-plate of the PCA, no DC voltage will be applied between the electrodes. An incoming terahertz wave will then be measurable as an induced voltage in the substrate which is illustrated in figure 2.6.

Optical Rectification

A second method which is used for generation of THz-pulses is commonly known as optical rectification, but a more accurate description would be calling it difference-frequency generation. As can be seen from figure 2.7 a pulsed laser-source propagates through a nonlinear optical crystal having a sufficiently large $\chi^{(2)}$, due to the finite duration of the pulse it contains a certain band of frequencies, as shown for stimulated Raman in figure 2.4b. These frequencies interact by means of difference-frequency generation (DFG), thereby resulting in a terahertz pulse. The main limitation for frequency bandwidth of generated THz-pulses is the temporal time duration of the ultrafast laser-source. More precisely it depends on the tranform limited temporal pulsewidth. This is because a shorter pulse coming from the laser will contain a broader spectrum of frequencies.

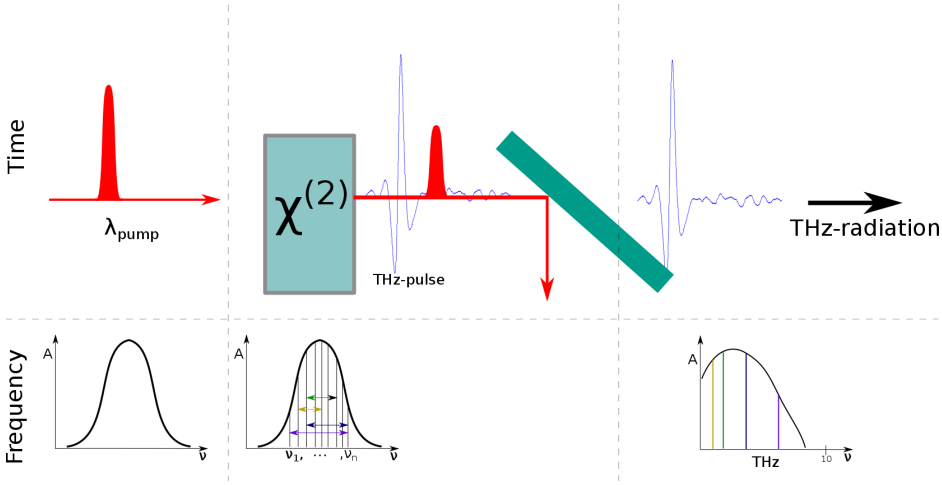

Figure 2.7: Difference-frequency generation terahertz pulses

Free space plasma generation

A third method creates terahertz pulses by means of interactions in generated air-plasma [21]. The excitation pulse passes through a SHG crystal, converting part of the energy into its second-harmonic (e.g. $\lambda = 400$nm for a $\lambda = 800$nm pulse). Plasma is created in the focal point for the two beams due to a very high electric field amplitude. The 800 and 400 nm waves interact, some experimental studies suggests that the THz-generation in air is due to the third-order nonlinear phenomenon called four-wave mixing (FWM) [22]. And explains the generation of THz-waves as caused by ponderomotive forces, however the exact physical explanation of the THz generation in plasma is still under investigation. The SHG crystal is not necessary for the plasma to emit THz radiation, but greatly enhances the generated pulse [23]. The resulting THz-radiation propagates in the direction of initial beam. This field has unknown polarization so for most optical setups some sort of linear polariser is used. The spectrum of the THz-wave is directly dependent on the temporal pulselength of the femtosecond pulse similarly to the other techniques mentioned previously. Another aspect is that only a few percent of the fs laser pulse is converted to the terahertz wave. As described by Xie et al [22] the generated THz-field can be described as:

$$E_{THz} \propto \chi^{(3)} \sqrt{I_{2\omega}} I_{\omega} \cos(\phi) \tag{2.26}$$

Where I_{ω} and $I_{2\omega}$ are the optical intensities of the fundamental and second-harmonic frequencies respectively. The relative phase difference is given as ϕ. Different strategies have been researched to try to improve this yield, as typically just a few percent of the optical power is converted into the THz-wave. Chen et al. came up with such a method [24], and managed an increase to about 150% by generating multiple plasmas and by superimposing these. As mentioned

previously, in the case of PCAs they might be used for both generation and detection of THz-waves. Dai et al. investigated the possibility of using free-space plasma in a similar fashion, by using it for detection as well as generation [25]. Free space plasma used for detection, albeit interesting is not commonly used in THz-setups.

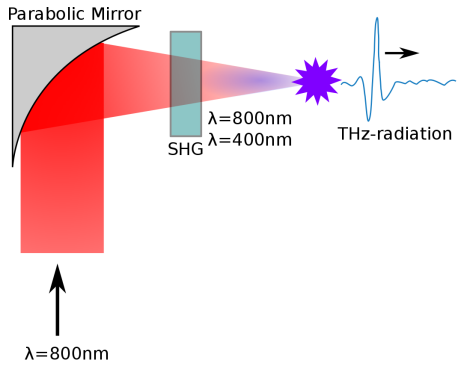

Figure 2.8: Free space plasma generation

2.1.5 Electro-Optic Detection

One way of measuring pulsed signals that has been used frequently is the electro-optic detection scheme. The idea is to use one probe beam which is typically weak, and one pump or excitation beam, most often from the same laser source. The pump beam will in practice induce the signal which is to be measured. The fundamental idea of this method is to use a nonlinear optical crystal to measure the pump beam by considering the induced change in refractive index, this might be due to either the Pockels effect, or by the optical Kerr effect. Therefore this change in refractive index is either dependent on the electric field strength, or the intensity correspondingly. For a Pockels-type detection the setup is as follows; the probe and the pump are focused onto a nonlinear crystal, typically a ZnTe. It is essential that they overlap both spatially in the crystal, along the whole length, and in time. Given that the pump beam is present it will then induce an increased refractive index along its polarization axis, giving rise to a birefringence in the crystal. Therefore by measuring this refractive index change one is able to measure the E-field or intensity of the signal. A schematic of a typical setup is shown in figure 2.9. If no signal is present the probe will pass through the EO-crystal maintaining its original linear polarization, however if a signal is present the induced birefringence will cause a polarization shift. After the crystal aside from typically a set of focusing lenses and guiding elements it will pass through a quarter-wave-plate changing its polarization from linear to elliptical. In the special case of probe polarization being 45° on the fast and slow axes of the QWP, which is the initial configuration when no signal is present in the EO-crystal, the resulting polarization would be

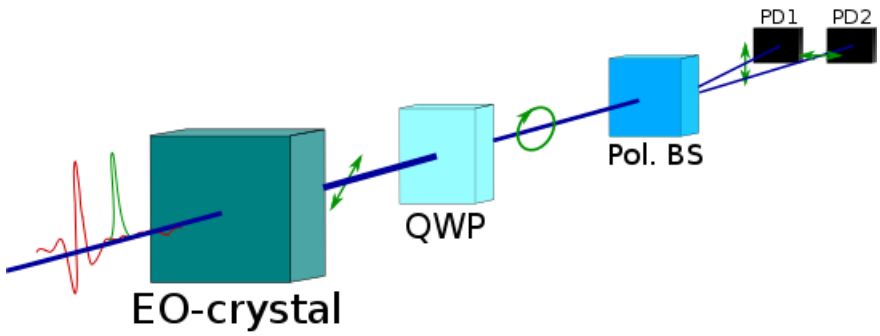

Figure 2.9: Electro-optic detection, probe and pump are spatially overlapping inside the crystal. Quarter wave plate (QWP), polarizing beam-splitter, photodiodes 1 and 2

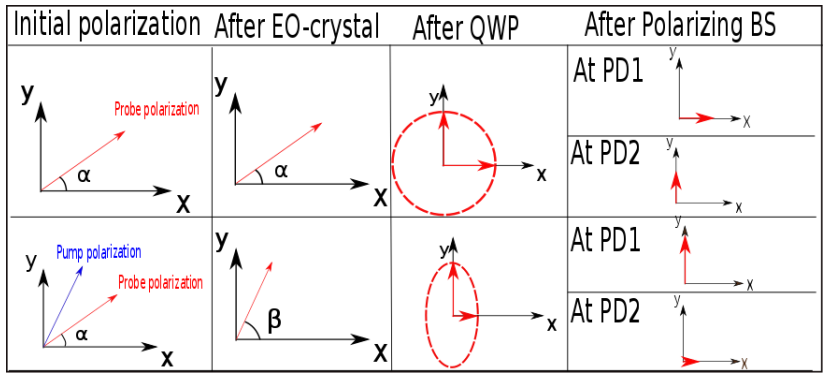

Figure 2.10: Probe polarization as it propagates through an electro-optic detection configuration

circular. The optical element following is a polarizing beamsplitter, such as a Wollaston prism. The prism will redirect the beam according to its polarization directions, and these two polarization directions will in turn be detected by two photodiodes. Balanced detection is commonly used to give an output signal which corresponds to the difference between intensities at the two photodiodes $V_{out} = V_{p1} - V_{p2}$. As the intensities at the two photodiodes are directly corresponding to the polarization directions, this difference is proportional to the birefringence in the EO-crystal. As can be seen from this equation the output given by the original circular probe will be zero. On the other hand if the signal to be measured is present in the crystal this will change the probe polarization due to the induced birefringence. After the QWP the probe would obtain an elliptical polarization, resulting in different intensities at the two photodiodes, thus an output signal $V_{out} \neq 0$ would be obtained.

The resulting measured electric field-strength in the case of THz-detection as

described by Skjeie [26]:

$$\mathrm{E}_{THz} = \frac{2\Delta V}{V_{max}} \cdot \frac{c}{\omega n_0^3 r_{41} d} \tag{2.27}$$

where ΔV is the measured voltage difference between the photodiodes and V_{max} being the corresponding maximum produced voltage. While c is the speed of light in vacuum, ω the probe frequency. n_0 is the refractive index of the EO-crystal, in this particular case a ZnTe which has the electro-optic coefficient r_{41}, and a thickness d.
For the whole pulse to be measured a translation stage is needed to change the optical delay of the probe pulse relative to the pump. This requirement is illustrated by the OKE and THz-TDS setups in the coming sections. By having a pump arriving at the EO-detecting crystal constant and varying the delay of the probe, it enables overlapping between the two at various positions. The measurement at each specific delay will correspond to one discrete data-point, which in practice represents a convolution relationship between the pump and probe pulses. As a consequence one may increase the time-resolution of the measured pulse-shape by using smaller steps.

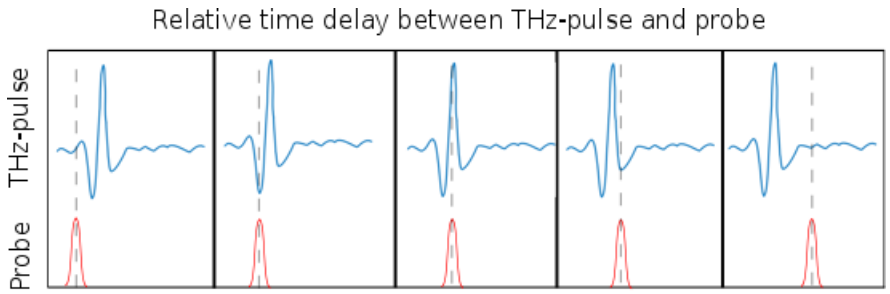

Figure 2.11: Measurement of pulse transient by using a translation stage

2.1.6 Lock-in Amplifiers

To enable measurements of very weak signals it has been found that utilizing a chopper frequency locked to a lock-in amplifier greatly increases SNR. The principle is using phase-sensitive detection to exclude signals not corresponding to the reference frequency, this makes for a truly narrow frequency-band. The phase sensitive detected voltage is the multiplication of the reference with detected signal [27]:

$$V_{psd} = V_{sig}V_L \sin(\omega_t t + \theta_{sig}) \sin(\omega_L t + \theta_{ref})$$

$$= \frac{V_{sig}V_L \cos[(\omega_r - \omega_L)t + \theta_{sig} - \theta_{ref}]}{2} - \frac{V_{sig}V_L \cos[(\omega_r + \omega_L)t + \theta_{sig} + \theta_{ref}]}{2} \tag{2.28}$$

where V_L, ω_L and θ_L is the amplitude, angular frequency and phase for the lock-in amplifier. V_{psd} is passed through a low-pass filter, in the special case of $\omega_r = \omega_L$, the resulting signal is nonzero. $V_{psd} = \frac{V_{sig}V_L \cos(\theta_{sig} - \theta_{ref})}{2}$
For dual-phase lock ins (using two phase-sensitive detectors (PSD)), the resulting signal is composed of two parts:

$$X = V_{sig} \cos(\theta) \qquad Y = V_{sig} \sin(\theta)$$

$$R = V_{sig} = \sqrt{X^2 + Y^2} \tag{2.29}$$

2.2 Material

2.2.1 Crystallographic Orientation

For crystalline materials a common way to describe their symmetry axis and orientation is by looking at the Miller indices as shown in figure 2.12. The Miller indices have the *hkl* notation and defines the reciprocal lattice vector describing the orientation of groups of crystalline planes: $\mathbf{g}_{hkl} = h\mathbf{b_1} + k\mathbf{b_2} + l\mathbf{b_3}$, where $\mathbf{b_1}, \mathbf{b_2}$ and $\mathbf{b_3}$ are the reciprocal lattice vectors which are directly linked to the real space lattice vectors $\mathbf{a_1}, \mathbf{a_2}$ and $\mathbf{a_3}$ describing the unit cell [28].

$$\mathbf{b_1} = 2\pi \frac{\mathbf{a_2} \times \mathbf{a_3}}{\mathbf{a_1} \cdot (\mathbf{a_2} \times \mathbf{a_3})}, \mathbf{b_2} = 2\pi \frac{\mathbf{a_3} \times \mathbf{a_1}}{\mathbf{a_2} \cdot (\mathbf{a_3} \times \mathbf{a_1})}, \mathbf{b_3} = 2\pi \frac{\mathbf{a_1} \times \mathbf{a_2}}{\mathbf{a_3} \cdot (\mathbf{a_1} \times \mathbf{a_2})} \tag{2.30}$$

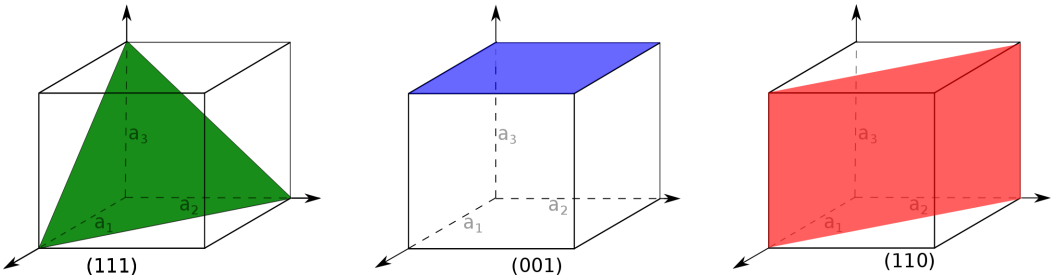

Figure 2.12: Miller indices

2.2.2 Ferroelectric Effect

Solid state materials might exhibit a variety of properties due to the different symmetries and configurations belonging to the various space and room groups. Some of these have been used to a great extent in sensing and actuation. Piezoelectricity is the ability for a material to exhibit a built up electrostatic potential when an external stress is applied. And reversely a voltage may be applied to the piezoelectric crystal for it to be deformed. One example of devices which often uses piezoelectrics for sensing and actuation are the micro-electro mechanical systems (MEMS), as traditional mechanic solutions at the microscale often have restrictions not seen for macroscopic devices such as stiction and reliability of moving parts. Some materials exhibiting peizoelectricity might also by pyroelectrics, which implies that heat can induce an electrostatic potential in the material. A subgroup of the pyroelectrics are the ferroelectrics. Out of the 230 point groups only 10 of these show pyroelectric behaviour, as only a fraction of pyroelectrics are ferroelectrics it implies that ferroelectricity is a relatively rare material property. What makes ferroelectrics differ from the more common dielctrics and paraelectrics is that if a coercive field of sufficient strength is applied across the material this will cause it to show a permanent state of polarization. In dielectrics and paraelectrics a polarization will be built up in the material when an electric field is applied, but when the field is removed, the polarization relaxes to its equilibrium position at $\mathbf{P} = 0$. For ferroelectrics on the other hand the polarization follows a hysteresis curve, with two possible polarization states at zero applied electric field as shown in figure 2.13c. These states might be flipped by applying an opposite coercive field, thus it is easy to imagine how these two states might be utilized for binary systems and information storage. There exists two possible reasons for ferroelectricity which makes for the classifications: order-disorder and displacive [28]. The ferroelectric effect is dependent on some inherent non-symmetry in the crystal, since a permanent charge displacement in the crystal is required, as this is the causing the non-relaxing polarization. However, a ferroelectric material might not hold on to this property as the temperature increases above a certain threshold. If one imagines that a centre atom in a cubic crystal unit structure is displaced, such as the green Ti atom in figure 2.14, when heat is applied to the system this atom will vibrate, as it will occupy a higher energy state. When this vibration is large enough the atom in this case would no longer be confined to one of these two positions which is the causing the ferroelectricity, meaning that at a certain temperature the material would cease to be a ferroelectric, this transition temperature is called the Curie temperature T_c. There exists a number of aspects which in turn has effect on the ferroelectricity, some of the most central being temperature and stress/strain. The latter has been under thorough investigation as these could be inherent in the material or be induced at the interfaces of other materials [8], for thin-films stress due to crystalline mismatch or defects might cause this to play an even bigger role due to the limited thickness.

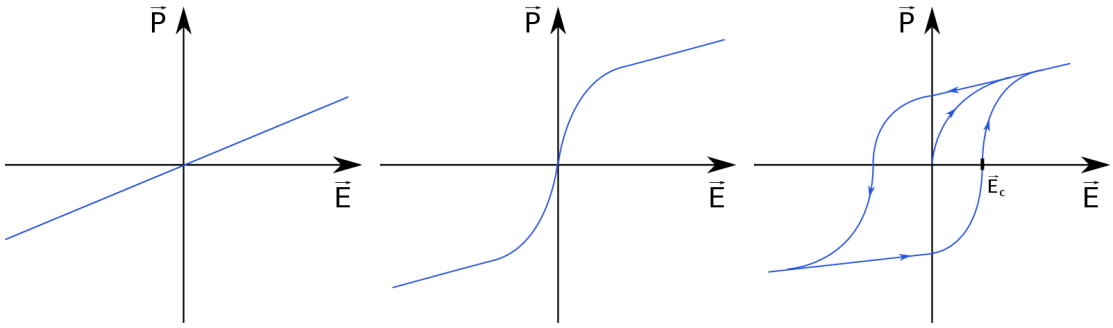

(a) Dielectric (b) Paraelectric (c) Ferroelectric

Figure 2.13: Polarization vs. electric field for dielectrics, paraelectrisc and ferroelectrics

Perovskites

One particularly interesting group of materials are the perovskites, these have a structure as shown in figure 2.14, ABO_3. The reason why researchers have placed a particular interest in this group is due to their various piezo- and ferro-electric as well as ferromagnetic properties. Some well known perovskites are barium titanate $BaTiO_3$ (BTO), strontium titanate $SrTiO_3$ (STO) and the much used piezoelectric $Pb(Sr, Zi)TiO_3$ (PZT). The ferromagnetic $(La, Sr)MnO_3$ (LSMO) has also been under extensive research due its ferromagnetic properties. The structure can be described as follows; at the faces the cation B can be found: being the oxygen atoms, in the body center the anion titanate atom is located, while the A cation such as barium or strontium can be found in the corners.

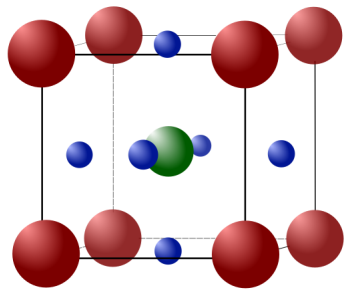

Figure 2.14: Crystal structure $BaTiO_3$, the red corner atoms are barium, oxygen in blue at the face center positions and titanium in the centre coloured green

2.2.3 Crystallographic phases

Solids are classified in different groups depending on crystalline symmetry. However, as can be seen for BTO in fig. 2.16 a material might not be limited to one crystalline symmetry, but display structural phase transitions at various temperatures. As can be seen from the figure, BTO has a tetragonal structure at room temperature, but loses this symmetry thus also its ferroelectric properties at high temperatures when it goes to being cubic. STO on the other hand has a cubic crystalline structure at room temperature. At the transition temperature T_c at 105K it changes from cubic to tetragonal [29]. Three common crystalline phases are shown below in figure 2.15.

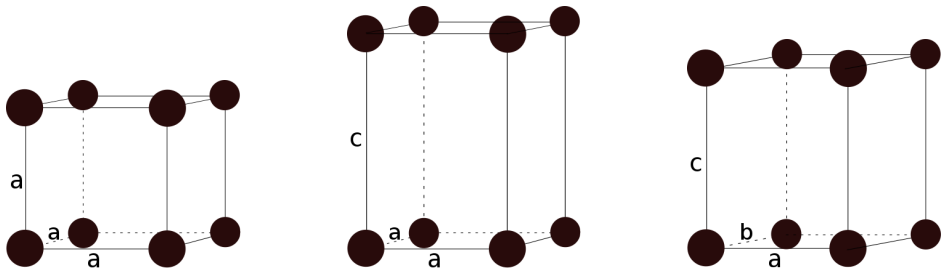

(a) Cubic symmetry, all sides have equal length

(b) Tetragonal symmetry, $a \neq c$

(c) Orthorombic symmetry, $a \neq b \neq c$

Figure 2.15: Crystalline symmetry

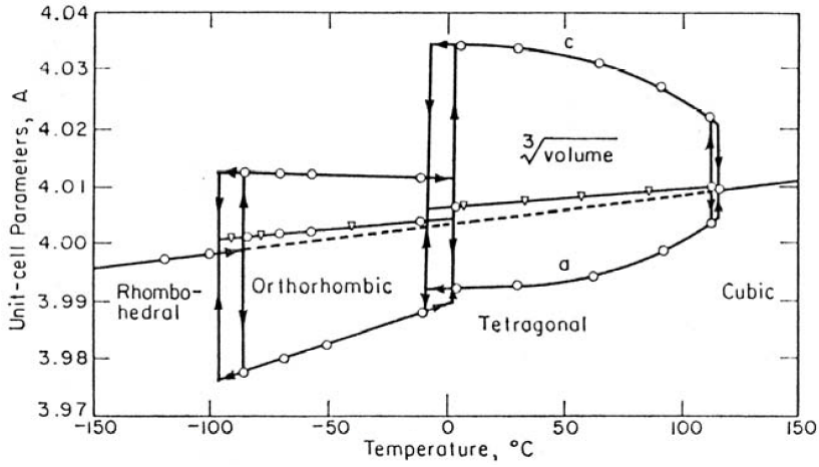

Figure 2.16: $BaTiO_3$ crystalline phase dependence on temperature, figure from Jona et al. [30]

2.2.4 Phonons

The phonon-modes in materials corresponds to allowed motions or vibrational states of atoms in the crystalline lattice. These phonons may propagate in the material and are characterized as quantized particles, similarly to the photon for electro-magnetic waves. Since the density of states for the phonon modes is directly related to the thermal properties of a solid, it makes knowledge of available phonon states and phonon-interactions important for understanding contributing factors for the material dependent thermal and electrical conductivity. These vibrations can be described in a simplified form by using the Lorentz oscillator model, where a mass is oscillating around its equilibrium position. Phonons are in general classified into two main groups; the optical and the acoustic phonon-modes. Which are divided into another subgroup of being either longitudinal or transversal. The difference between acoustic and optic phonons is illustrated in figure 2.17, where the black solid line corresponds to the equilibrium position of the atoms, while the green and red corresponds to different charges.

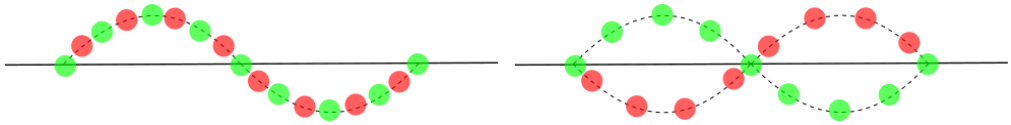

(a) Acoustic phonon (b) Optical phonon

Figure 2.17: Acoustic and optical phonons, where red and green illustrates atoms of different charge

As can be seen from figure 2.17, the atoms in an acoustic phonon are displaced in phase independent of atomic charge. For optical modes however, one can see a π phaseshift, meaning that positive and negative charges oscillate out of phase. A common way to describe the optical and acoustic modes in a material is to plot the corresponding dispersion relation $\omega(k)$ as illustrated in figure 2.18.
The photon-phonon interaction can be modelled similarly to the classical dipole oscillator model as described in section 2.1.1. By using figure 2.17 the red and green circles can be seen as corresponding to polar unit cells. For light to be able to interact with a phonon in a material, the material itself need to show some polar properties. This is due to conservation laws for the momentum, as the phonon and photon must have same wave vector and frequency. A further implication of this criterion is that incoming EM-waves can only directly be absorbed by transverse optical (TO) phonon modes. The corresponding complex dielectric function can be calculated to determine material properties such as absorption and refractive index in a similar fashion as shown earlier:

$$\epsilon_r(\omega) = 1 + \chi + \frac{Nq^2}{\epsilon_0 \mu} \frac{1}{(\Omega_{TO}^2 - \omega^2 - i\gamma\omega)} \tag{2.31}$$

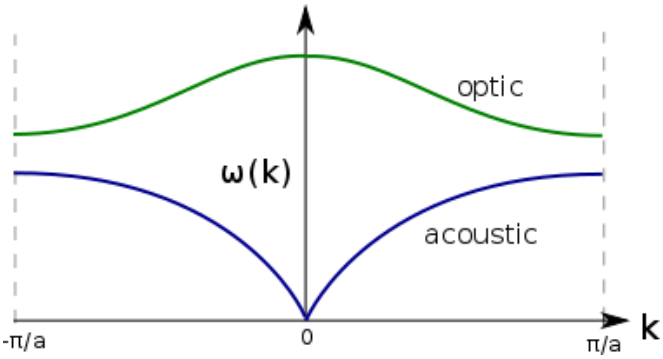

Figure 2.18: Dispersion-relation showing frequency dependence on wavenumber $k = 2\pi/\lambda$

which simplifies to

$$\epsilon_r(\omega) = \epsilon_\infty + (\epsilon_{st} - \epsilon_\infty)\frac{\Omega_{TO}^2}{(\Omega_{TO}^2 - \omega^2 - i\gamma\omega)} \tag{2.32}$$

where ϵ_∞ and ϵ_{st} are the high and low frequency limits respectively, but still far from the next resonance. From this it can be seen that for lightly damped systems at specific frequency one obtains the Lyddane-Sachs-Teller (LST) relationship:

$$\frac{\Omega_{LO}^2}{\Omega_{TO}^2} = \frac{\epsilon_{st}}{\epsilon_\infty} \tag{2.33}$$

The LST relationship can also be used as a tool for understanding how certain physical properties affect each other, such as how condensation of a TO mode would affect the dielectric permittivity. Another important aspect of the LST, is that it enables calculation of Ω_{LO}, the frequency of the longitunal optical phonon mode. In practical experiments this is of significant importance due the region in between Ω_{TO} and Ω_{LO} displaying a reflectivity approaching unity. This region is known as the "Reststrahlen" band, and has a high reflectivity due to the dielectric permittivity being negative [15]. For transmission experiments this would imply that depending on the location and bandwidth between the LO and TO mode this could severely limit the obtainable spectral information, this would be particularly limiting if the material exhibit a multiple of excitable phonon modes in the measured spectral range.

Some phonon modes may be of particular interest due to how they give rise to certain material properties, one such example is how the TO1 mode in some perovskites are directly related to ferroelectricity. From an experimentalists point of view, enabling the extraction of such phonon information could make for a qualitative tool for understanding and customize production of these materials for further research.

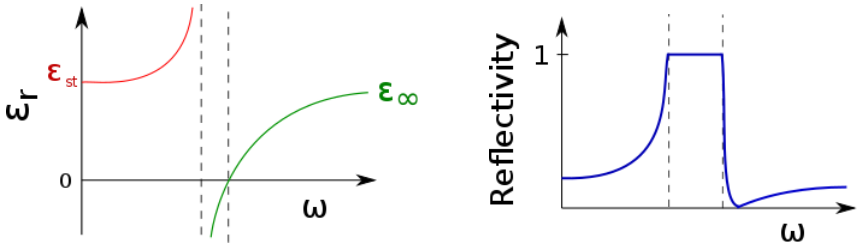

(a) Dielectric function around phonon resonance

(b) Typical reflection behaviour around phonon resonance

Figure 2.19: Around phonon resonance

Phonon-structural phase relationship

Crystalline symmetry can be described in terms of its free energy. This gives rise to the Landau theory of phase transitions, where the preferred crystalline symmetry is determined by lowest available free energy of the system [28]. For a phase-transition such as the cubic-tetragonal for $BaTiO_3$ as shown in figure 2.16 it could be illustrated in the following manner. Two different crystalline symmetries will have temperature dependent free energy A and B as shown in figure 2.20. This is illustrated by the line corresponding to the cubic symmetry A, and the tetragonal B. At high temperatures T$> T_c$ the solid is symmetry B, due to the lowest free energy. As can be seen from the plot, at a specific temperature T_c the lines intersect and at T$< T_c$ the tetragonal phase has the lowest free energy, thus a phase-transition occurs. For ferroelectrics this transition region T_c is of special interest due to a couple of reason. Most importantly it determines in which temperature region the material displays ferroelectric properties. The behaviour at T_c is additionally used to classify the dielectric. If the soft-phonon can propagate, it is called a displacive ferroelectric (because of the atom causing polarization states has been displaced and condensate). Before this structural phase transition the contributing phonon-mode will be softened, leading to further displacement of the atom, and a lowering in frequency will be seen until it approaches zero, causing it to condensate into one of the fixed position corresponding to energy minima.

Quasi-modes

Due to the nature of the phonon-modes one often observe combination modes when doing experimental measurements, or the so-called quasimodes. This lack of direct observation at the true phonon frequencies makes for the need of developed models which enables extraction of these contributing modes. This requires thorough understanding of both the experimental set-up, in terms of directionality of interacting waves, polarizations, sample symmetry, active phonon modes, and the directionality of these in comparison to each other. Here the case of BTO will be more thoroughly discussed based on the work by Fontana et al.

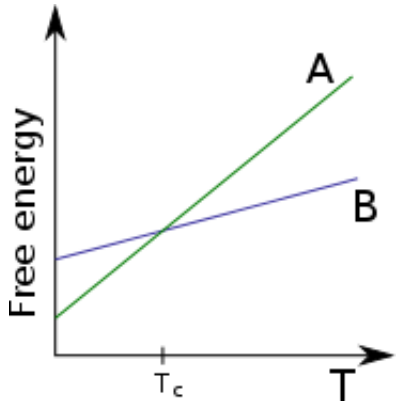

Figure 2.20: Temperature dependent crystalline symmetry

[13]. BTO has a tetragonal structure at room temperature as shown in figure 2.16, and belongs to the point-group C_{4v} and has two contributing phonon modes A_1 and E. The A_1 is in the a-a crystalline plane, while E is along the c-direction. As will be shown in the OKE section, for an incoming wave coming perpendicularly at a BTO thin-film grown on a <111> STO, it would see both the A_1 and E phonon-modes, and thereby resulting in a quasi-mode. Fontana describes briefly a model which can be used to extract the information about the real phonon frequencies in his paper where he uses Raman spectroscopy for studies of BTO. It takes into account the quasimode frequencies and uses this to determine the frequencies of the contributing modes:

$$\epsilon_c(\infty)\cos^2(\theta)\sum_j[\omega_{A1}^2(LO_j)-\omega_\theta]\sum_j[\omega_E^2(TO_j)-\omega_\theta^2]+\epsilon_a(\infty)\sin^2\theta\sum_j[\omega_E^2(LO_j)-\omega_\theta^2] \times\sum_j[\omega_{A1}^2(TO_j)-\omega_\theta^2]=0 \tag{2.34}$$

Where θ is the angle of the incoming wave relative to the crystalline <100> direction. The subscripts a and c indicate the directions in for a tetragonal symmetry can be seen in figure 2.15b. It was found that this equation did not give satisfying accuracy for determining the $BaTiO_3$ phonon modes when comparing with existing literature. However by using a modified version inserting a damping constant γ_E it was found to correspond well with reported values.

$$\epsilon_a(\omega)=\frac{\epsilon_a(\infty)\left(\sum_j[\omega_E^2(LO_j)-\omega^2]\Big/\sum_{j\neq1}[\omega_E^2(TO_j)-\omega^2]\right)}{\omega_E^2(TO_1)-\omega^2+\imath\omega\gamma_E(TO_1)} \tag{2.35}$$

This gives the quasimode dispersion, which can be used to obtain the various phonon modes:

$$\epsilon_c(\infty)\cos^2\theta[[\omega_E^2(TO_1)-\omega_\theta]^2+\omega_\theta^2\gamma_E^2(TO_1)]\sum_j[\omega_{A1}^2(LO_j)-\omega_\theta^2]\sum_{j\neq 1}[\omega_E^2(TO_j)-\omega_\theta^2]$$
$$+\epsilon_a(\infty)\sin^2\theta[\omega_E^2(TO_1)-\omega_\theta^2]\left(\sum_j[\omega_E^2(LO_j)-\omega_\theta^2]\sum_j[\omega_{A1}^2(TO_j)-\omega_\theta^2]\right)=0 \tag{2.36}$$

Chapter 3

Experimental Part I: Optical Kerr Effect Spectroscopy

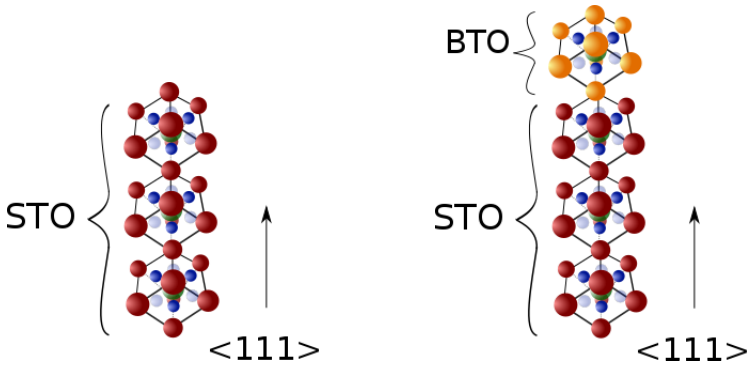

(a) $< 111 > SrTiO_3$ substrate

(b) $BaTiO_3$ thin-film on top of $< 111 > SrTiO_3$ substrate

Figure 3.1: Crystalline structures of the samples

3.1 Sample Preparation

The first STO substrates used for this study had one side polished, since truly smooth surfaces are needed for deposition of high quality thin-films. The other side had significant inherent surface roughness. In case of THz-TDS this would presumably have little to no effect on the measurements as will be discussed later. For OKE on the other hand this is likely to play a significant role. Since the laser wavelength is centred at $\lambda = 800nm$, having roughness in the μm region was demonstrated to cause massive scattering. This indicated that samples therefore needed to undergo polishing in order to become measurable, resulting in the need

for a polishing procedure of these perovskite substrates to be established.

3.1.1 Polishing:

After a thorough study it was found that using a rough paper in the beginning, gently polishing until the peaks were no longer as visible, followed by a very fine more heavy handed polish produced the best result. Due to the roughness of the first paper, an additional feature of the polish would possibly be a slight reduction in sample thickness. The samples were glued to a metal sample-holder for easier handling as illustrated in figure 3.2. At this stage it was crucial to place the samples at centre-position of the holder to avoid any unevenness of polish or causing tilt when doing more aggressive polish. The quality of polishing and surface roughness were both assessed by visual inspection, either by looking at light-reflection from the surface or by using an optical microscope.

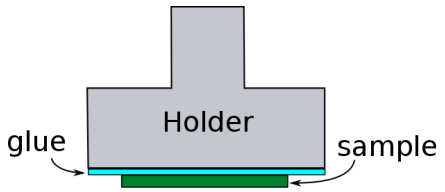

Figure 3.2: Sample holder for doing polishing

3.2 Principle of OKE

The basic need for doing ultrafast spectroscopy is a pulsed laser, emitting pulses having a temporal pulsewidth short enough to enable measurement at the desired timescale and frequency range. The need for short temporal pulses to enable probing broad bandwidths comes from the relationship between the two $\Delta f_{pulse} \propto 1/\tau_{pulse}$. Even with the continuous-wave (CW) lasers developed in the 60s, it was not until the 80s that lasers with pulsewidths in the femtosecond range was achieved. This enabled the study of ultrafast phenomena, typically how a system behaves after being excited by a source, be it chemical processes, luminescence properties or atomic orientational dynamics [31]. In addition to the improved time-resolution, the strong electric field of the pulse, enables nonlinear optical phenomena to occur and be used for spectroscopic purposes. Optical Kerr effect spectroscopy (OKE) uses the third-order nonlinear phenomena which the name suggests.

OKE is a pump-probe technique, meaning that a pump beam is used for either generation of the desired signal, or to cause change in material properties due to light-matter interaction. The probe on the other hand is used solely for measurement purposes. OKE all revolves around measuring the polarization shift of the probe, this shift originates from the induced birefringence Δn, which is

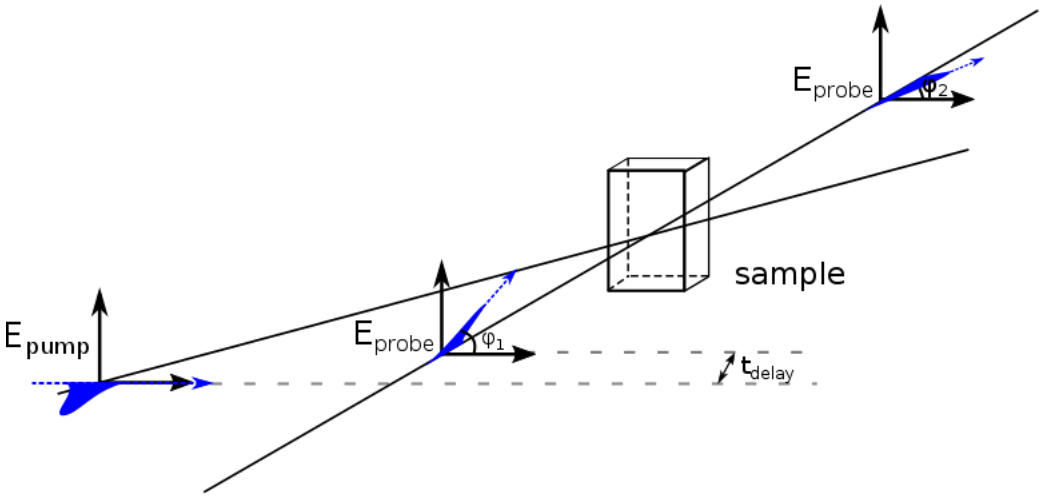

Figure 3.3: Principle of Optical Kerr Effect Spectroscopy

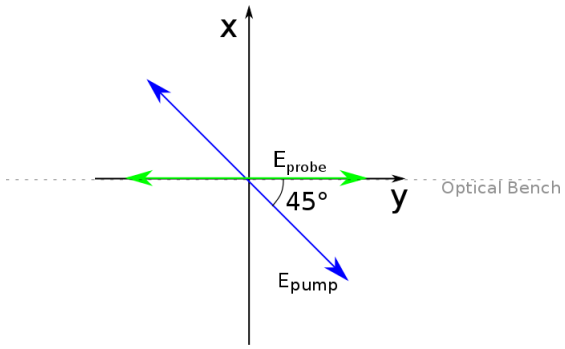

Figure 3.4: Pump-probe polarizations for this particular setup for a pulse propagating in the z-direction

caused by the optical Kerr effect, ultimately a result of the excitation by the pump.
The detected polarization change is due to induced birefringence in the material. As shown in the theory section for a given third order nonlinear process the susceptibility is given as $\chi^{(3)}_{ijkl}$. The polarization which fulfils the frequency relationship for the optical Kerr effect is given as:

$$P_i^{(3)}(\omega_s = \omega_{pu} - \omega_{pu} + \omega_{pr}) = \epsilon_0 \left(\chi^{(3)}_{ijkl} E_j(\omega_{pu}) E_k(-\omega_{pu}) E_l(\omega_{pr})\right) \tag{3.1}$$

For this particular setup as shown in figure 3.4 the probe is linearly polarized in the horizontal direction, at an angle 45° relative to the pump polarization. The subscripts as described earlier indicate the cartesian coordinate axes: along x is 1, along y is 2. For the formulas below the following notation is used for the

ordering of subscripts: Given χ_{ijkl}: i resulting signal polarization, j and k are pump polarizations, while l is the probe. This results in the following formulas for the polarizations:

$$P_1^{(3)}(\omega_s = \omega_{pu} - \omega_{pu} + \omega_{pr}) = \epsilon_0 \left[\chi_{1122}^{(3)} E_1(\omega_{pu}) E_2^*(\omega_{pu}) E_2(\omega_{pr}) + \chi_{1212}^{(3)} E_2(\omega_{pu}) E_1^*(\omega_{pu}) E_2(\omega_{pr})\right] \tag{3.2}$$

$$P_2^{(3)}(\omega_s = \omega_{pu} - \omega_{pu} + \omega_{pr}) = \epsilon_0 \left[\chi_{2112}^{(3)} E_1(\omega_{pu}) E_1^*(\omega_{pu}) E_2(\omega_{pr}) + \chi_{2222}^{(3)} E_2(\omega_{pu}) E_2^*(\omega_{pu}) E_2(\omega_{pr})\right] \tag{3.3}$$

Experimental Setup:

An ultrafast laser-source emits pulses having a temporal pulsewidth in the range of 80fs, at a repetition rate of 1 kHz. This is split into two paths as illustrated in figure 3.5, a pump and a probe pulse. To have complete control of the transmitted optical power of the two paths a set of adjustable intensity-filters have been implemented not shown in the figure. The pump pulse passes through an optical chopper, connected to a lock-in amplifier to enable very sensitive detection. It is then redirected through the optical system by a set of mirrors, before going through a linear polarizer. The linearly polarized pump is then focused by a lens hitting the sample in the focal plane. Light-matter interaction between the pump pulse and sample induces a refractive index change along the pump polarization caused by the optical Kerr effect. At last the transmitted pump pulse is blocked after having propagating through the sample.
The probe pulse used to measure the signal is directed to a computer controlled translation stage, changing the relative time-delay between pump and probe. The probe then passes through a linear polarizer obtaining a polarization direction 45° relative to the pump, before being focused by a lens, overlapping with the pump inside the sample. Until at last passing through the QWP and Wollaston prism, which makes for EO-detection, and at last measured by means of balanced detection. A requirement for the probe is that it needs to have weak intensity compared to the pump in order to avoid any self-induced nonlinear optical effects. Typically the ratio between pump-probe in regards of optical power is at a minimum 80:20 [18],[35],[34]. In the following experiments pump/probe ratio is typically better more than 30:1.

3.3 Heterodyne Detection

Detection of an OKE signal can be done by using either homodyne or heterodyne detection [32]. The principle of heterodyne detection is to use a local oscillator E^{lc} to superimpose with the signal field, this is typically achieved by using a quarter-wave plate. The resulting signal from these two configurations can be

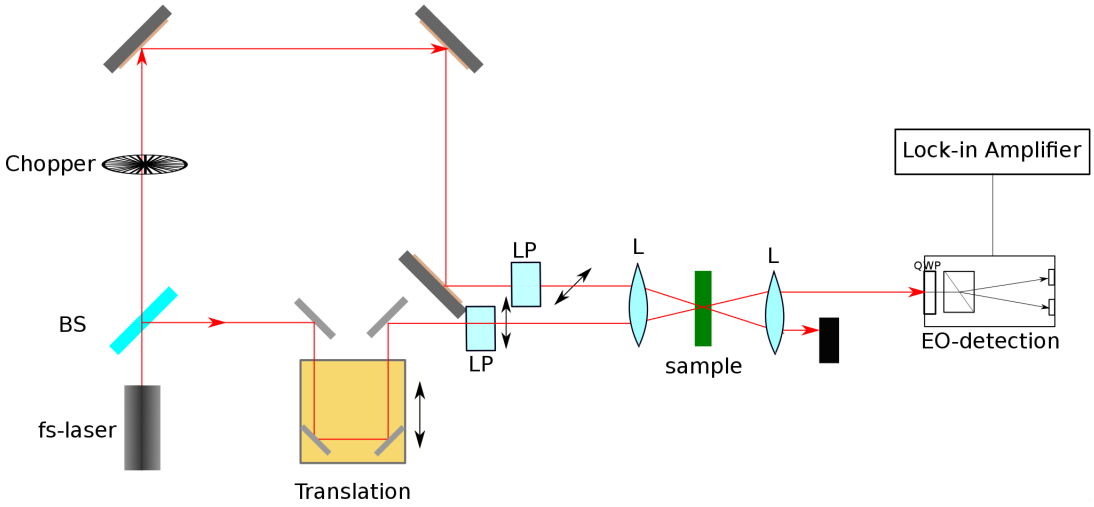

Figure 3.5: OKE setup

described as:

$$S_{homo}(\tau) \propto \int |E^{sg}(t)|^2 dt \propto \int dt \mathcal{I}(t-\tau) \left[\int dt' \mathcal{R}_{OKE}(t-t') \mathcal{I}(t')^2 \right] \tag{3.4}$$

$$S_{hete}(\tau) \propto \int dt \mathcal{I}(t-\tau) \int dt' \mathcal{R}_{OKE}(t-t') \mathcal{I}(t') \tag{3.5}$$

where E^{sg} is the signal field. As can be seen for the heterodyne detection, the resulting signal has a linear relation to the material response function R_{OKE}, which is what makes this method highly preferable.
A more precise description for the setup commonly used is optical-heterodyne detection optical Kerr effect spectroscopy (OHD-OKE).

3.4 Data Preparation and Processing

3.4.1 Data Preparation

The data obtained from the OKE setup comes from the lock-in amplifier, measured by means of phase-sensitive detection as described in section 2.1.6. It consist of amplitude information in the form of x and y components, as well as the corresponding positioning of the translation stage causing the relative time-delay between the pump and probe pulses. Since the data from the lock-in uses a default phase constant for signal calculations it requires post-processing to find the optimal phase. The data preparation can be described in the following steps:

1. Load the raw data measured by the lock-in amplifier.
2. Find the maximum amplitude of the signal by varying the phase $0 \leq \phi \leq 2\pi$, for the x and y components.
3. Adjust amplitude data to compensate for initial offset caused by static noise
4. Normalize the data with respect to peak amplitude

3.4.2 Curve-fitting

The retrieved signal in OKE is as mentioned previously caused by optical Kerr effect induced birefringence in the sample, in other words a refractive index change along the polarization direction of the pump. Various contributions makes for the detected OKE transient, which properties will soon be discussed in more detail. In general the detected signal from an OKE measurement can be divided into regions attributed to the various physical effects dominating. Around zero time delay, both the pump and probe are temporally overlapping inside the sample. This results in a signal mainly caused by displacement of electron clouds and nuclei, the electron response is very rapid while the nuclear response is slower due to its larger mass. For liquids the interacting EM-wave may also cause molecular rotation and libration [33],[34], as they will try to align along the polarization direction of the pump, this is typically visible as a slowly relaxing tail displaying exponential decay in the picoseconds-range. Determining the relaxation dynamics on a picoseconds timescale is one of the major advantages of OKE. Quitevis et al. [35] published one of the early papers on using curve-fitting for extracting information on these relaxation processes. It has been found that for OKE measurement the relaxation can usually be curve-fitted by either a single or double exponential:

$$A \cdot \exp^{\frac{-t}{\tau_i}} (1 - \exp^{\frac{-t}{\tau_r}}) \tag{3.6}$$

Where A is the amplitude, τ_i is the relaxational time-constant, τ_r is an arbitrary rise-time. The exact value of τ_r has been found not to be of vital importance for long range fitting, but it is typically chosen to be in the range of 10-200fs [36], [37].

3.4.3 Retrieving spectra

Theoretical foundation:

McMorrow et al. discovered that the OKE experiments not only allowed for the study of ultrafast temporal dynamics in materials, but contained in addition valuable spectral information [38]-[39]. It was found that by using the properties of Fourier transform on the time-domain signal one is able to obtain the Raman spectrum directly. The following derivation of the relationship between the measured OKE transient and the frequency-domain signal follows the original paper by McMorrow and Lotshaw [38].

The refractive index in an OKE experiment for transparent media can be described as follows:

$$n_{OKE} = n + \Delta n \tag{3.7}$$

where n is the linear refractive index along the polarization direction of the pump, and Δn is the induced refractive index change caused by the optical Kerr effect as described previously, which is related to the material response:

$$\Delta n(t) = \delta n_{\parallel}(t) - \delta n_{\perp}(t) = \int_{-\infty}^{t} dt^{'} \Phi_{ijkl}^{Re}(t - t^{'}) I_{pump}(t^{'}) \tag{3.8}$$

With I_{pump} being the intensity envelope of the pulse, $\Phi_{ijkl}(t)$ is called the NLO polarization impulse response function, and is directly related to the material response function $R_{ijkl} = \Phi_{ijkl}^{Re}$. The imaginary part Φ_{ijkl}^{Im} is on the other hand related to field-matter interaction in terms of energy exchange. The parallel and orthogonal refractive index change is given relative to the pump polarization direction. In general a material excitation is given by:

$$Q(t) = \int_{-\infty}^{t} dt^{'} \Phi_{ijkl}(t - t^{'}) E_k^*(t^{'}) E_l(t^{'}) \tag{3.9}$$

$$\Phi_{ijkl}(t) = \Phi_{ijkl}^{Re}(t) + i\Phi_{ijkl}^{Im}(t) \tag{3.10}$$

For transparent materials it can be shown that the NLO impulse response function can be separated into electronic and nuclear contributions by the following relation:

$$\Phi_{ijkl}(t) = \sigma_{ijkl}(t) + \Phi_{nuc}(t) \tag{3.11}$$

with the electronic hyperpolarizability given as:

$$\sigma_{ijkl}(t) = b\delta(t) \tag{3.12}$$

By using heterodyne detection it can be shown that the measured time-domain signal may be described as:

$$T(\tau) = \int_{-\infty}^{\infty} G_0^{(2)}(\tau - t) \Phi_{ijkl}^{Re}(t) dt = G_0^{(2)} * R_{ijkl}(\tau) \tag{3.13}$$

where $G_0^{(2)}$ is the zero-background intensity autocorrelation of the excitation pulse. This quantity simply contains the information of the pump pulse. In an experimental setting $G_0^{(2)}$ may be measured directly by using a SHG crystal at the sample position. The Fourier transform of the material response function is defined as:

$$D_{ijkl}(\Delta\omega) = \int_{-\infty}^{\infty} R_{ijkl}(t) e^{i\Delta\omega t} dt = \mathcal{F}[R_{ijkl}(t)] \tag{3.14}$$

by using the properties of Fourier transform and combining equation 3.13 and 3.14 this gives:

$$D_{ijkl}(\Delta\omega) = \frac{\mathcal{F}(G_0^{(2)}(\tau))\mathcal{F}(R_{ijkl}(\tau))}{\mathcal{F}(G_0^{(2)}(\tau))} = \frac{\mathcal{F}(T(\tau))}{\mathcal{F}(G_0^{(2)}(\tau))} \tag{3.15}$$

which ultimately leads to the separation of nuclear and electronic contributions to the spectrum:

$$\Im D_{ijkl}(\Delta\omega) = \Im\mathcal{F}(R_{nuc}(t)) \tag{3.16}$$

The electronic hyperpolarizability only affects the real part of the FT material response:

$$\Re D_{ijkl}(\Delta\omega) = b + \Re\mathcal{F}(R_{nuc}) \tag{3.17}$$

This developed procedure by McMorrow and Lotshaw resulted in a way to directly measure the low-frequency Raman spectrum using OHD-OKE. In literature the retrieved spectrum is often called the total spectral density (TSD):

$$\Im D(\omega) = \Im\left[\frac{\mathcal{F}(S(\tau))}{\mathcal{F}(G_0(\tau))}\right] \tag{3.18}$$

a variety of notations for the contributing parts are used. The part used as a reference for retrieving the Raman spectrum is often called the instrument function, above denoted $G_0(\tau)$.

Some materials might exhibit slowly relaxing contributions to the nuclear response. In some cases it is desirable to remove this slowly reorientational contribution when calculating the Raman spectrum. The Raman spectrum obtained from a time-domain signal with these slowly relaxing components removed is called the reduced spectral density (RSD) [36]. A comparison between the total spectral density and reduced spectral density can be seen for acetone in figure **??**.

Pratical Considerations:

The implications of the total spectral density calculation is the requirement of a reference signal to enable measurement of the Raman spectrum. Typically a SHG crystal is placed within the setup and used to measure the intensity autocorrelation function at the sample positon, and further used as the instrument function in the Raman spectrum calculations. In the case of thin-films deposited on top of a substrate material or other two-layered samples, a method of retrieving the Raman spectrum would be to measure the pure substrate separately and use this as the instrument function, to solely have contributions of the thin-films. One of the challenges when doing OKE is choosing a suitable region of the time-domain signal for retrieving a reliable Raman spectrum. As no standard procedures exist, the choices made should be justified based on

qualitative understanding of the OKE transient, nevertheless it adds some uncertainty in regards to the obtained Raman spectrum. Because of the measurement for the sample and instrument-function not being done simultaneously there exists a possibility for the measured peak positions to be slightly displaced to each other. By doing relative shift in the post-processing this displacement can be compensated, the effect of these relative shifts is shown in the discussion section. As can be seen from the plots, this relative time-shift between the pulses affects significantly the peak-positions in the retrieved Raman spectrum. Generally one should take notice that the temporal pulsewidth seen at the sample position is not the same as the output of the laser due to the pulse travelling through a range of optical elements. These makes for dispersion and thereby temporal broadening of the pulse. This can be compensated by applying a negative chirp to the output pulse from the laser if such an option is available. Another way of obtaining an instrument function instead of measuring the intensity autocorrelation is by using a Gaussian approximation. Doing this Gaussian approximation of the intensity autocorrelation may be used yields reasonable results, given that the temporal pulsewidth at the sample-position is known.

3.4.4 Retrieving third-order susceptibility

A parameter of interest which can be directly retrieved from an OKE measurement is the material dependent third order susceptibility $\chi^{(3)}$. By using a material with a known $\chi_r^{(3)}$ as the reference, and do comparisons between the measured maximum peak amplitudes of the OKE transients, the sample susceptibility $\chi_s^{(3)}$ can be determined. Since the induced birefringence is proportional to the intensity of the pump it is crucial that both the sample of interest and the reference has the same experimental conditions. The most common method is using the same pump-intensity, I_{pump}, for both measurements which gives the following relationship [40]-[41]:

$$\chi_s^{(3)} = \chi_r^{(3)} \left(\frac{I_s}{I_r}\right)^{1/2} \left(\frac{L_r}{L_s}\right) \left(\frac{n_s}{n_r}\right)^2 \frac{\alpha L}{e^{-\alpha L/2}(1-e^{-\alpha L})} \tag{3.19}$$

where I_s and I_r are the intensities for sample and reference respectively, L_r and L_s are the corresponding OKE interaction lengths, typically chosen as the sample and reference thickness. n_s and n_r are the linear refractive indices at λ_{pump}, while the corresponding absorption coefficient for the sample given as α. If the sample is particularly absorbing it might become necessary to use a higher intensity pump $I_{s,pump}$ compared to the intensity used for the reference measurement $I_{r,pump}$. Assuming the length of the sample and reference is similar, $L_r = L_s$, another formula might be used to calculate $\chi_s^{(3)}$ [42]:

$$\chi_s^{(3)} = \chi_r^{(3)} \left(\frac{I_s}{I_r}\right)^{1/2} \left(\frac{I_{r,pump}}{I_{s,pump}}\right)^{3/2} \left(\frac{n_s}{n_r}\right)^2 \frac{\alpha L}{e^{-\alpha L/2}(1-e^{-\alpha L})} \tag{3.20}$$

For an accurate calculation of the third order susceptibility the reflection at the various interfaces needs to be taken into account. As can be seen in equation 3.19 and 3.20, the calculation greatly depends on the intensity of the pump interacting with the sample. In case of thin-film measurements the reflection at the interfaces contribute to an intensity decrease of the pump before it reaches the material of interest is illustrated in figure 3.6a. This is caused by difference in refractive index and can be calculated by using the well known Fresnel equations. Reflection at an air-sample interface for an incoming wave at normal incidence can be described as:

$$R = \frac{(n-1)^2 + \kappa^2}{(n+1)^2 + \kappa^2} \tag{3.21}$$

where n is the refractive index of the medium, and κ being related to the absorption coefficient $\kappa = \frac{\lambda\alpha}{4\pi}$

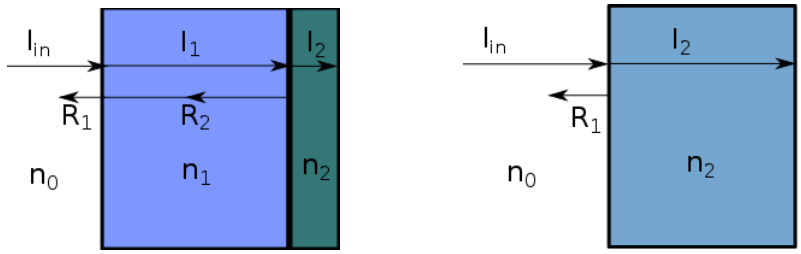

(a) Thin-film on substrate (b) Pure substrate

Figure 3.6: Reflection at the interfaces

Typical values for the experimentally determined third-order susceptibilities can

Sample material:		**Refractive index:**	**Calculated** $\chi^{(3)}$ [esu]:
Strontium titanate	$SrTiO_3$	2.3422	$1.98 \cdot 10^{-13}$
Acetone	$(CH_3)_2CO$	1.3547	$2.3 \cdot 10^{-14}$

Table 3.1: Measurement of of third-order susceptibility determined by OKE

be found in table 3.1, based on reported values for the refractive indices at the pulse wavelength $\lambda = 800nm$ [43], where the absorption coefficient in $SrTiO_3$ is approximate to zero [44]. By using CS_2 as a reference with $\chi^{(3)}_{CS_2} = 0.67 \cdot 10^{-13}$ (esu) the third order susceptibility of acetone was obtained, which further enabled extraction of $\chi^{(3)}_{STO}$.

3.5 Experimental Results

3.5.1 Acetone

An OKE measurement for acetone can be seen in figure 3.7. Around t = 0 the pump and probe pulses partially overlap inside the sample causing nuclear and electronic contributions to dominate, while the slowly decaying contribution coming after is caused by molecular reorientation [45]. To obtain the Raman spectrum as shown in figure 3.8, a Gaussian approximation was implemented for the instrument function. The slow relaxational component was curve-fitted to a double exponential and subtracted from the signal, to obtain the reduced spectral density. Implications of this subtraction will be shown in the following chapter. In the corresponding plot showing the calculated RSD for acetone, seen in figure 3.8, a main peak can be seen centred around $44cm^{-1}$. This peak location corresponds well with reported values found in similar studies [36].

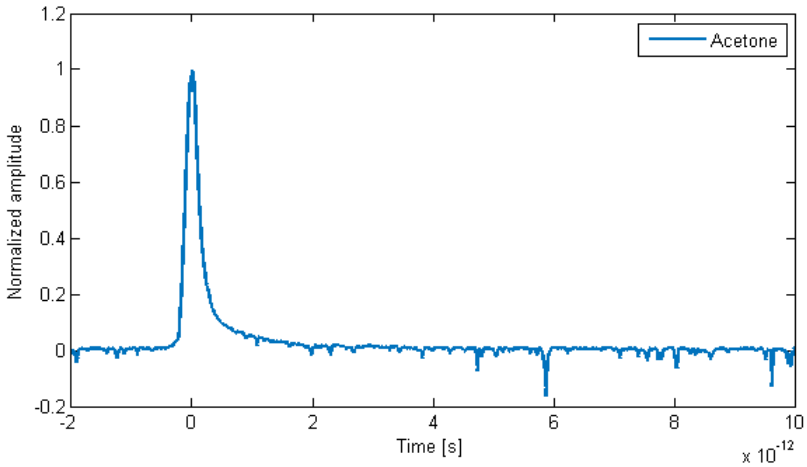

Figure 3.7: Measured time domain signal for pure acetone

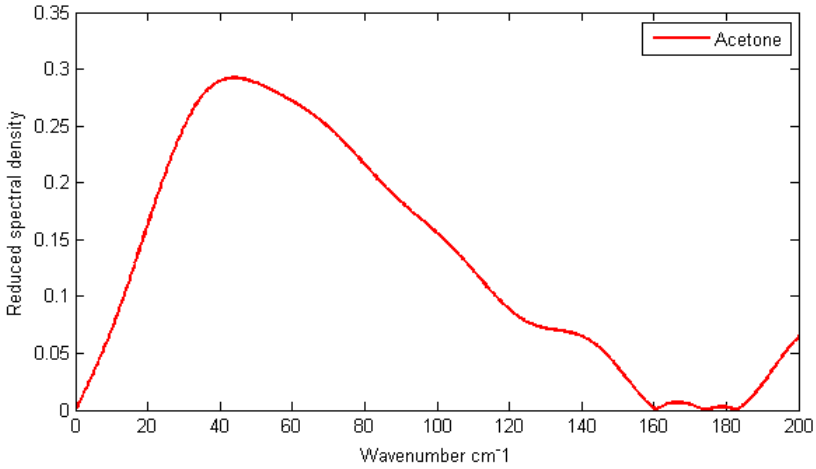

Figure 3.8: Retrieved Raman spectrum for acetone using OKE

3.5.2 Overview of $SrTiO_3$ and $BaTiO_3$ samples:

An overview of the measured samples can be seen in table 3.2. $BaTiO_3$ thin-films in the range of 10-100nm are grown on top of 500μm thick mono-crystalline <111> oriented $SrTiO_3$ substrates by means of pulsed laser deposition (PLD). This results in a <111> thin-film as it follows the substrate material. All of the following samples uses STO substrates having been factory polished on both sides except for *STO manual* where one of the sides has been polished by hand.

Appropriate sample size needed for the various measurements are mostly limited by practical concerns, since the size requirement to enable OKE measurements are typically in the μm-range. The default size for the substrates was chosen to be 5x5x0.5 mm. To reduce uncertainty for the THz-TDS measurements the *STO prepped* and *BTO 100* have dimensions 10x10x0.5 mm

For consistency all of the following measurements for THz-TDS and OHD-OKE were done in the same manner as shown in figure 3.9.

3.5.3 $SrTiO_3$ Substrate

The time signal for OKE measurements of the three substrate samples: *STO prepped*, *STO chamber* and *STO manual* can be seen in figure 3.10.

Sample name	**Deposited thin-film**	**Subst. mat.**	**Processing steps**
STO manual	None	$SrTiO_3$	Manually polished - no chemical steps or annealing
STO prepped	None	$SrTiO_3$	US bath - acetone and methanol - HF, Annealing
STO chamber	None	$SrTiO_3$	Same as prepped - placed in deposition chamber
BTO 10	10nm $BaTiO_3$	$SrTiO_3$	Same as STO chamber with PLD deposition of BTO
BTO 20	20nm $BaTiO_3$	$SrTiO_3$	Same as STO chamber with PLD deposition of BTO
BTO 100	100nm $BaTiO_3$	$SrTiO_3$	Same as STO chamber with PLD deposition of BTO

Table 3.2: Overview of various samples used for THz-TDS and OKE

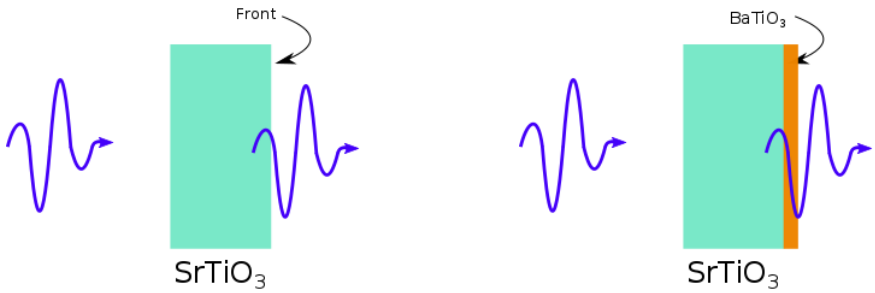

(a) Substrate measurements (b) Thin-film measurements

Figure 3.9: Measurement configuration for THz-TDS and OHD-OKE

The corresponding calculated Raman spectrum was retrieved by using a Gaussian instrument function and subtracting the non-relaxing contribution which can be seen between the main and second peak. The corresponding RSD plot has peak values in the region of 84-86 cm^{-1} which proximity to the reported Raman-peak at 90 cm^{-1} suggest that this could be an observation of the TO1 phonon-mode in $SrTiO_3$ [46].

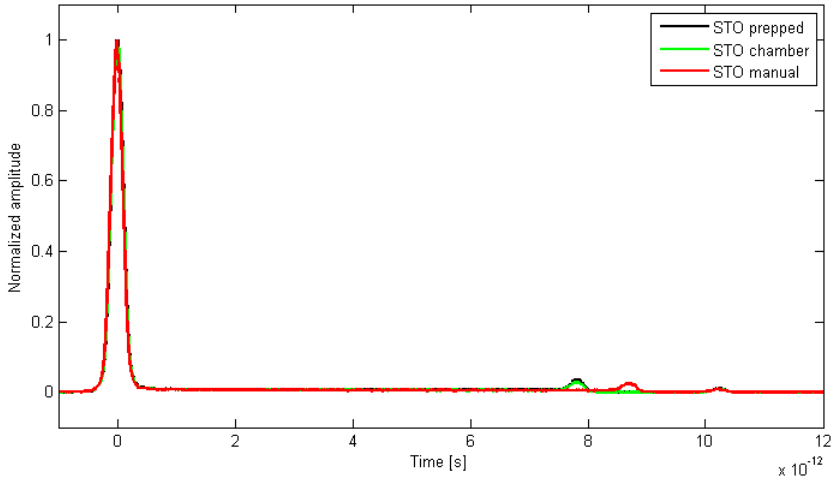

(a) Linear

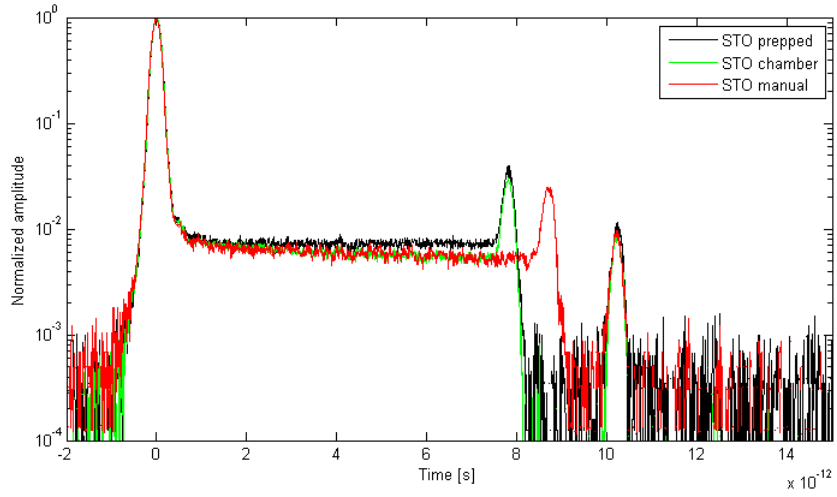

(b) Semi-logarithmic

Figure 3.10: OKE time-domain measurements of STO

Influence of relative rotations

An incoming wave would ideally have an optical axis being parallel to the <111> crystal planes following the z-axis in figure 3.12. To determine if the STO samples showed any anisotropic behaviour the angle dependence of the measured peak value of the OKE signal was investigated. This was achieved by rotating the sample around the optical axis, which would cause the relative orientation of the

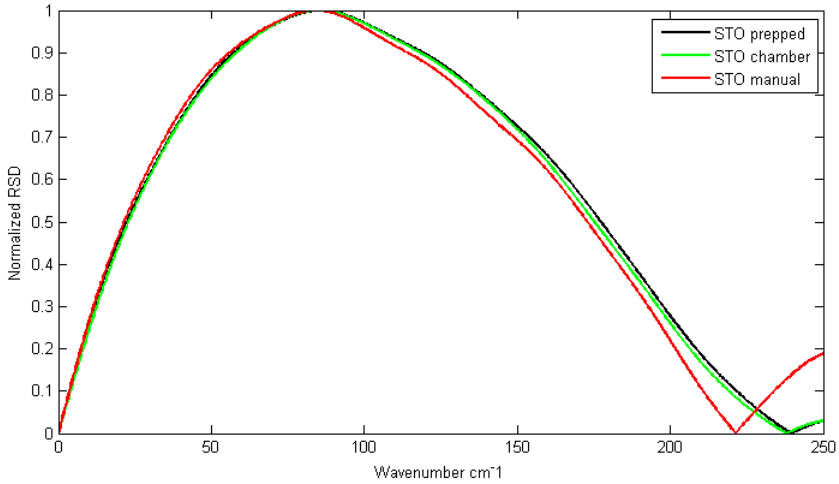

Figure 3.11: Raman spectrum for various STO samples (RSD)

pump polarization in regards to the crystalline axes to change. This resulted in the plot shown in figure 3.13, measured for *STO prepped*.

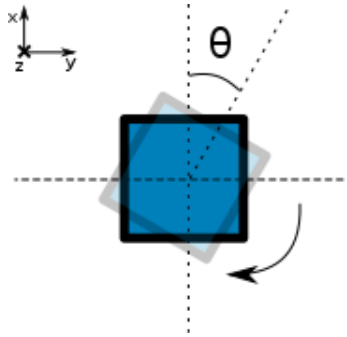

Figure 3.12: Rotation around optical axis

The incoming pulse is assumed to propagate into the plane, perpendicularly to the <111> direction.
The measurements were performed using $P_{pump} \sim 4mW$, and $P_{probe} \sim 150\mu W$.

3.5.4 $BaTiO_3$ thin-film measurements

Time-plots of the retrieved OKE measurements of BTO thin-films of various thickness can be seen in figure 3.14.
The Raman spectrum calculations were found to be highly dependent on which part of the time-domain signal were chosen when calculating $\Im D(\omega)$. For the

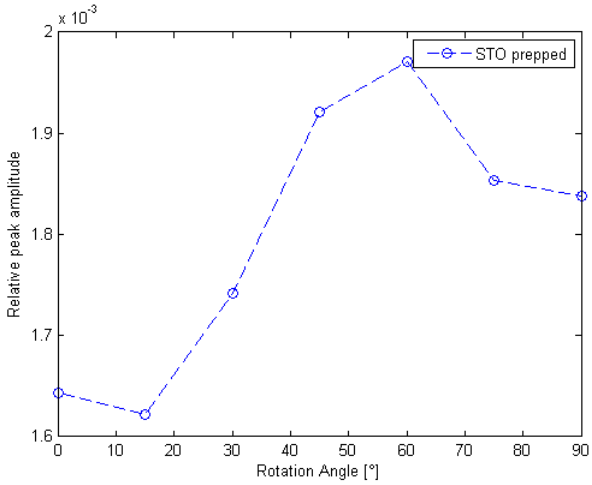

Figure 3.13: Measured peak values for *STO prepped* as a function of rotation around the optical axis

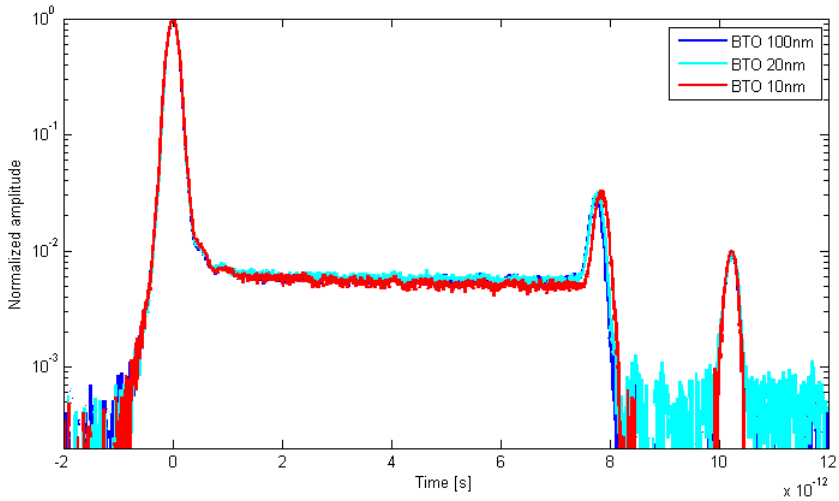

Figure 3.14: Measured time-domain signals for various BTO thicknesses

acetone and STO Raman spectra obtained in the previous sections, the signal information corresponding to the region from t= 0 ps was chosen, yielding satisfying results.

An example of a *BTO 100* measurement, using the same criteria can be seen below in figure 3.15, where there could be seen additional variations between measurements.

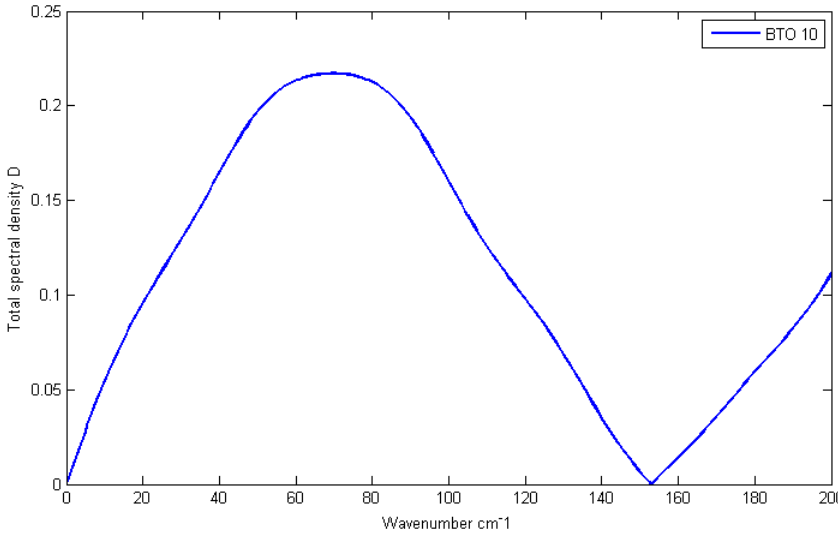

Figure 3.15: Raman spectrum from t=0 ps *BTO 100*

If the part appearing before the maximum peak amplitude were included in the calculations, typical plots shows behaviour as can be seen in figure 3.16. This sharp peak-position as can be seen, around $150cm^{-1}$ could possibly be related to the quasi-mode seen in BTO, as a combination of the A_1 and E phonon modes, as discussed in section **??**.

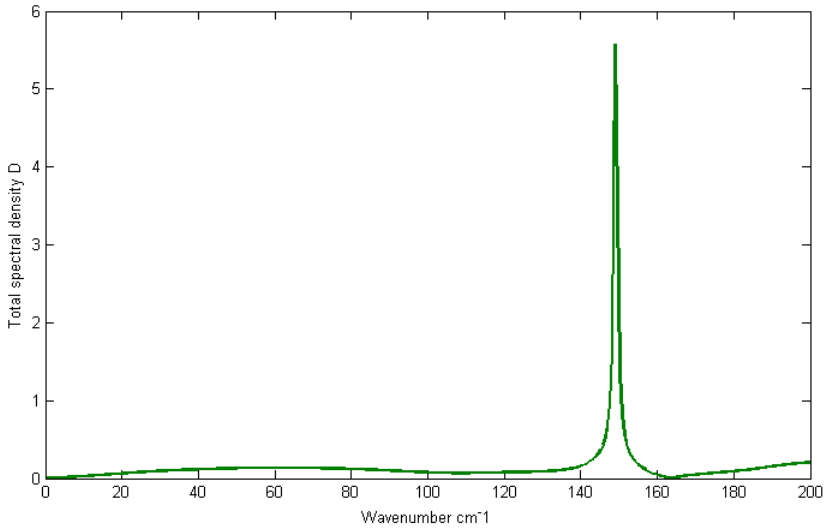

Figure 3.16: Raman spectrum calculating from t=-0.4 ps for *BTO 100*

Chapter 4

Experimental Part II: Terahertz Time-Domain Spectroscopy

4.1 Sample Preparation

Since the same samples were used for both the THz-TDS and OKE this implies that all samples used for THz-TDS have smooth surfaces on both sides. For experimental purposes it should be mentioned that the inherent surface roughness causing undesired light scattering in the OKE would be considered unlikely to have any significant effect in a terahertz time-domain spectroscopy measurement. As the wavelengths corresponding to the typical frequency bandwidth 0.2-6 THz would have wavelengths in the range $\lambda \sim 50 - 300\mu m$ and be considered spatially broad in comparison to the expected inherent surface-roughness of the substrate. Similarly to the OKE doing measurements on a sample material and comparing it with a high quality reference under similar experimental conditions is equally important in THz-TDS. An overview of the samples can be found in table **??**. An additional difficulty working with wavelengths being located in the far IR, such a terahertz waves, is the inability to easily trace the beam through an optical set-up. This is a result of the beam not being detectable by any conventional IR sensor card, such as mid-IR or the near-IR cards which can be used to trace the $\lambda = 800nm$ coming out of the laser. To reduce uncertainty caused by the inability of knowing the exact position of the THz-beam in the THz-TDS set-up, a set of 10x10mm samples were used for the measurements described in this section, namely the *BTO 100* and *STO prepped*.

4.2 Principle of THz-TDS

Terahertz time-domain spectroscopy is another type of pump-probe technique. The information obtained by these measurements partly overlaps with OKE in regards to the Raman spectrum, although the methods for obtaining this result

differ quite significantly. The principle is based on using an ultrafast laser-source to generate THz-pulses, typically achieved by either free space plasma generation, optical rectification or PCAs as described earlier. The generated terahertz pulse is either transmitted through the sample, which is the configuration implemented in this study. Or the set-up can be built so that one measures the THz-pulse being reflected by a sample, commonly known as measuring in reflection mode. A measured signal will give information on how the particular sample interacts with the THz-pulse and enables extraction of various material parameters such as the frequency dependent absorption coefficient and linear refractive index. For materials exhibiting high absorption in the terahertz regime, such as water, reflection mode is often preferred [47], as transmission mode THz-TDS relies on some part of the pulse being able to propagate through the material. Transmission measurements are will suited for low-absorbing samples, and for sufficiently thin highly absorbing materials, such as thin-films deposited on top of a transparent substrate.

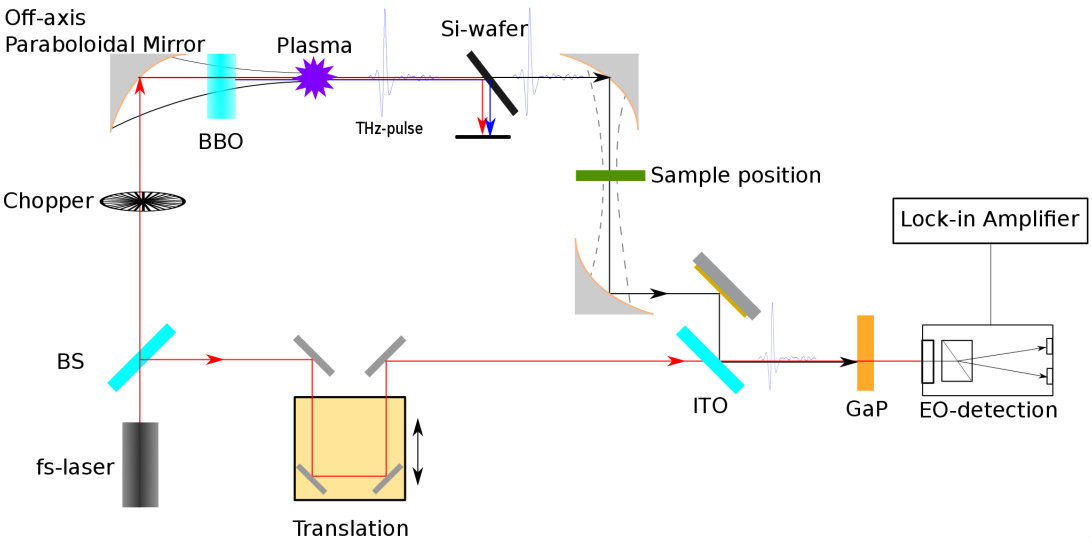

Figure 4.1: Experimental setup for THz-TDS

Experimental setup:

The experimental set-up is shown in figure 4.1. For generating and detecting the THz-pulses the principles of free-space plasma generation and electro-optic detection are implemented. A femtosecond laser source emits pulses with wavelength centred at $\lambda = 800nm$ having a FWHM pulse duration in the range of 100fs, and a repetition rate of 1kHz. This beam is split into two different optical pathways by the first beam splitter, a high-energy pump and lesser energy probe beam typically by a 80/20 BS. The strongest beam is used to generate the THz wave and passes through an optical chopper, which is frequency connected to a

lock-in amplifier, as discussed in section 2.1.6. Further it is reflected and focused by an off-axis paraboloidal mirror propagating through a nonlinear crystal, namely a $\beta-$ barium borate (BBO), converting part of the incoming $\lambda = 800nm$ wave into its second harmonic, $\lambda = 400nm$. These continue propagating until they reach the focal plane, causing ionization of the air, resulting in plasma generation and the creation of a THz-pulse. The first- and second-harmonic in addition to the THz-pulse continue to propagate through the system until they reach a silicon wafer. The wafer has to objectives, the first is to reflect the $\lambda = 400nm$ and $\lambda = 800nm$ so that only the THz-pulse is allowed to be transmitted. The second is working as a polarizer for the THz-pulse. Since a THz-pulse generated by the air plasma is assumed to have a random polarization, placing a Si-wafer at the Brewster angle causes the transmitted THz-pulse to have a mostly linear polarization, which is a necessity for being able to detect a signal using EO-detection. The next step is to focus the THz-pulse, placing the sample in Rayleigh-range of the focal plane. The transmitted pulse is redirected until it is reflected by an indium tin oxide (ITO) mirror, so that it eventually overlaps with the probe in a GaP-crystal causing birefringence due to the Pockels effect (EO-detection). The probe on the other hand passes through an optical delay line controlled by a PC, similarly to the OKE. It overlaps with the THz-pulse in the EO-crystal, before passing through a QWP and Wollaston prism, until finally being detected by a pair of photodiodes. The measured signal is directly corresponding to the E-field of the THz-pulse, containing both amplitude and phase information. This time-domain signal contains the corresponding frequencies in the range 0.2-6 THz, obtainable by Fourier transform.

What is not shown in figure 4.1 but is of vital importance in THz-TDS systems is that the system needs to be enclosed in a sufficiently air-tight chamber. Some groups purge the beam-path with nitrogen before doing measurements [48], another way of doing it which is implemented for this project is to dehumidify the air inside the chamber until it reaches an acceptable water concentration. A sufficiently low humidity was found to be in the range of $3-5\%$. The importance of having a low water concentration is due to the very high absorption by water in the THz-regime. Making water one of the most limiting factors for THz-wave propagation in practical applications.

In comparison to OKE where the Raman-active energy-modes are measured indirectly by the optical Kerr-effect and stimulated-Raman scattering, the THz-TDS is conceptually an easier method to obtain direct results. As the the measured transmitted signal through the sample is basically determined by absorption and reflection in the sample, one may be able to determine absorption bands directly by looking at the Fourier Transform of the time-domain signal.

4.3 Data Preparation and Processing

Similarly to the OKE setup, the THz-TDS setup uses EO-detection with a lock-in amplifier, and the data retrieved from the lock-in amplifier is processed in a similar fashion, please refer to section 3.4.1.

4.3.1 Retrieving Frequency Spectrum

The detected signal, as shown for air in figure 4.3, will be a direct measurement of the electric field amplitude and phase of the terahertz pulse. Relative time delay between detecting the THz-pulse for an air reference compared with a specific sample material will depend on the refractive index for the given material. The corresponding frequency information is retrievable by implementing a Fourier-transform converting the time-domain signal into the frequency-domain. Due to the measured data being a discrete measurement of the THz-pulse, it follows that a discrete Fourier Transform (DFT) is needed to extract the frequency information, which due to computational processing speed is implemented by a fast fourier-transform (FFT) algorithm.

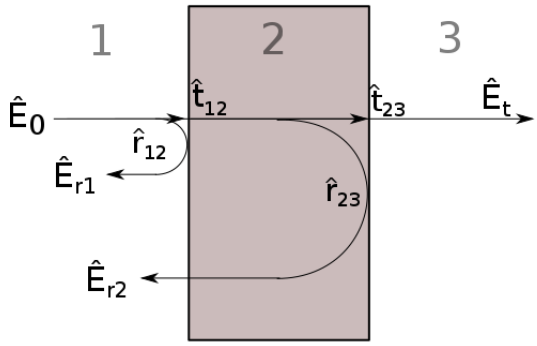

Figure 4.2: Fresnel reflection and transmission of tearhertz waves hitting a sample

As can be seen from figure 4.2 in the case of THz-TDS transmission measurement, the detected signal at the EO-detector does not only detect loss due to absorption in the sample, an equally important factor is the Fresnel reflection. The transmitted pulse can be described as:

$$\hat{E}_t(\omega) = \hat{E}_0 \hat{t}_{12} \hat{t}_{23} e^{-\alpha d/2} e^{\imath n \omega d/c} \tag{4.1}$$

where the Fresnel coefficients $\hat{t}_{12}$ and $\hat{t}_{23}$ describe the transmission due to reflection at the boundaries [20]. α is the frequency dependent absorption coefficient of the material and d being the sample thickness.

The information contained within a THz-TDS measurement can be extracted from the experimental transfer function:

$$\begin{aligned} H_{experiment}(\omega) &= \frac{\hat{E}_{sample}(\omega)}{\hat{E}_{ref}(\omega)} = T(\omega) e^{\imath \phi(\omega)} \\ &= \hat{t}_{12} \hat{t}_{23} e^{-\alpha d/2} e^{\imath (n-1) \omega d/c} \end{aligned} \tag{4.2}$$

4.3.2 Absorption coefficient and refractive index

Equation 4.2 gives the relationship between the experimental transfer function $H_{experiment}$ and the complex refractive index $\tilde{n} = n + i\kappa$, which gives the refractive index:

$$n(\omega) = 1 + \frac{c}{\omega d}\phi(\omega) \tag{4.3}$$

with the absorption coefficient:

$$\alpha(\omega) = -\frac{2}{d}\ln\left[T(\omega)\frac{[n(\omega)+1]^2}{4n(\omega)}\right] \tag{4.4}$$

where d is the sample thickness.

4.3.3 Valid spectral range

When obtaining the corresponding frequency spectrum for a specific sample depending on the spectral amplitudes it might not be easy to determine at which limit the obtained spectrum goes from being the actual signal measured to being noise. This may cause researchers to make wrong deductions from what is believed to be valid data, therefore a qualitative measure of valid spectral regions needed to be developed. This question was addressed by Jepsen and Fischer [49]. They found a qualitative way by looking at calculated absorption coefficient α and comparing this to the limit given by α_{max}, any absorption above α_{max} would imply that the spectrum is not valid.

$$\alpha_{max}d = 2ln\left(DR\frac{4n}{(n+1)^2}\right) \tag{4.5}$$

Where DR is the dynamic range, d is the thickness of the sample. A common way of defining the dynamic range for terahertz measurements is given as [50]:

$$\text{DR} = \frac{\text{maximum peak amplitude}}{\text{rms of noise floor}} \tag{4.6}$$

which can be compared with the more familiar signal-to-noise ratio (SNR):

$$\text{SNR} = \frac{\text{mean magnitude of amplitude}}{\text{standard deviation of amplitude}} \tag{4.7}$$

As mentioned by Jepsen, the α_{max} tells us limitation for spectral validity, but it was pointed out that this same limitation was not the same for the refractive index calculations..

4.3.4 Fabry-Perot Reflections for thin samples

If the sample is sufficiently thin then surface reflections needs to be taken into account when doing analysing the detected THz-pulse. As the sample thickness becomes comparatively thin to the THz-wave then reflection from the interfaces may no longer be seen as distinct peaks arriving at a certain time-delay after the main pulse, but may instead be superimposed in the main peak, causing interference effects. This can be described as [20]:

$$H(\omega) = \frac{\hat{E}_{sample}}{\hat{E}_{ref}} = \frac{4n}{(n+1)^2} e^{\alpha d/2} e^{in\omega d/c} \mathrm{FP}(\omega) \tag{4.8}$$

where $\mathrm{FP}(\omega)$ is the contribution caused by the Fabry-Perot reflections.

$$\mathrm{FP}(\omega) = \frac{1}{1 - \frac{n-1}{n+1} e^{-\alpha d} e^{2in\omega d/c}} \tag{4.9}$$

4.3.5 Developed Parameter Extraction Algorithm

The Matlab codes for calculating the refractive index, absorption coefficients as well as the transfer functions were implemented by Sørgård [51]. The main ideas for these feature extractions were based on the work by Pupeza et al.[52] and will now be briefly explained.
The idea behind feature extraction from these THz-TDS measurements is using the experimentally obtained transfer function $H_{experiment}$ and compare it to a theoretical transfer function H_{theory}. As it is directly dependent on the absorption coefficient $\alpha(\omega)$ and refractive index $n(\omega)$ of the sample, one may use this relationship in order to in order to optimize the theoretical transfer function, thereby inversely retrieving suitable values for $\alpha(\omega)$ and $n(\omega)$. The method calculates possible theoretical transfer functions for the various frequencies and iterates through possible variations to find a H_{theory} as close as possible to $H_{experiment}$. The quality of fit is determined by the calculation of corresponding error function:

$$M(\omega) = |H_{theory(omega)}| - |H_{experiment}(\omega)| \tag{4.10}$$

$$A(\omega) = \angle H_{theory(omega)} - \angle H_{experiment}(\omega) \tag{4.11}$$

$$Err = \sum_{\omega} (|M(\omega)| + |A(\omega)|) \tag{4.12}$$

4.4 THz-TDS: Air Reference

A THz-TDS measurement for air can be seen below in figure 4.3. The main pulse arrives at around 2 ps, the second peak which can be seen at around 8.5ps is due

to the reflection of the pulse in the GaP crystal. When choosing an appropriate region around the main peak, and running it through an FFT algorithm, the plot in figure 4.4 is obtained.

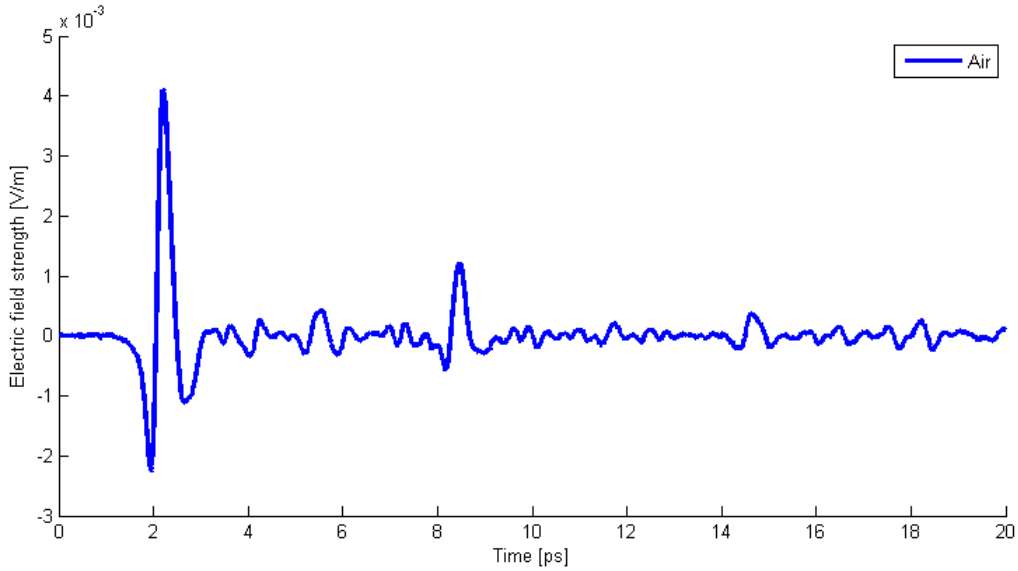

Figure 4.3: Measured THz-TDS signal for air

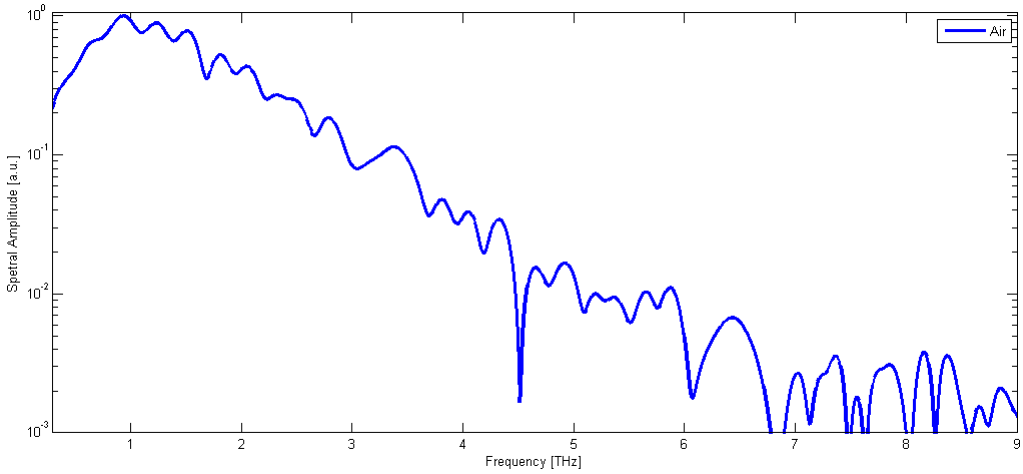

Figure 4.4: Corresponding THz-TDS spectrum for air

4.5 Experimental Results: $SrTiO_3$

For STO the corresponding refractive index and absorption coefficient was calculating using the obtained used air as a reference:

$$H_{experiment}(\omega) = \frac{E_{STO}(\omega)}{E_{air}(\omega)} \tag{4.13}$$

To enable determination of optical parameters for the various BTO thin-films it is crucial to get a good substrate measurement. As can be seen from figure 4.5 the measured electric field strength for STO is greatly influenced by the noise present in the system as it is truly weak. When comparing the plot of measured field strength of *STO prepped* to the corresponding air reference in figure 4.4 one can see that the maximum peak amplitude is less than 2.5% of the measured amplitude for air. This observation suggests that $SrTiO_3$ could possibly be highly absorbing in the THz-regime. To make sure that the lack of a sufficiently strong detected signal was not due to some experimental errors or unexpected material properties, a thorough study of various scenarios has been carried out, which will be explained in the discussion section. Since the retrieved signal is in the noise regime, showing measured electric field strength for the STO comparable to the spikes contributed by noise, the experimentally obtained material properties has significant uncertainties. Any of the following observations would need to be verified before any qualitative understanding of STO and BTO thin-films gained from these measurements can be established. A long range scan for the $500\mu m$ *prepped STO* substrate can be seen in figure 4.5.

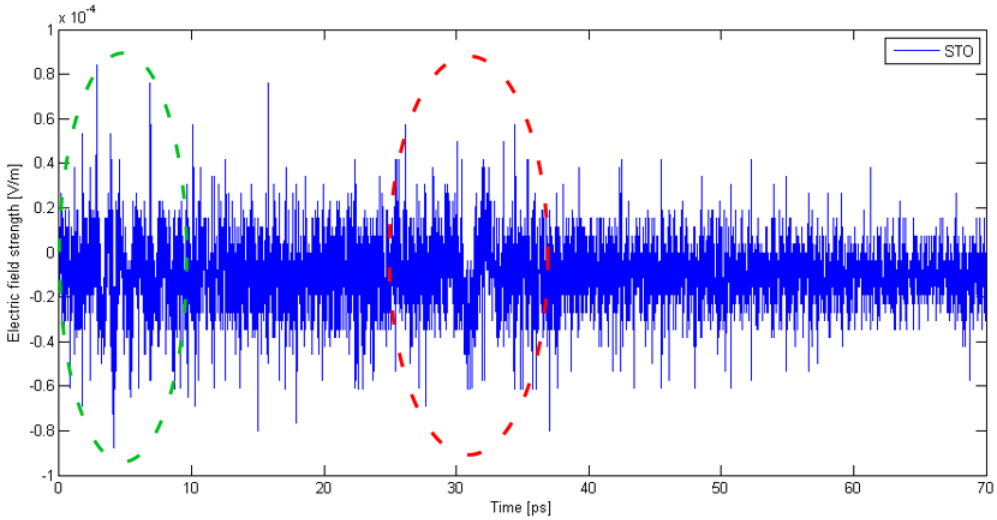

Figure 4.5: <111> grown $500\mu m$ STO substrate, scanned over a range of 70ps

Two regions were found to be of particular interest, as they show behaviour that resembles pulse-shapes. One can be seen around 4ps time-delay, the other

broader pulse-shape can be seen around 32ps. A better resolution plot of these regions can be seen below in 4.6.

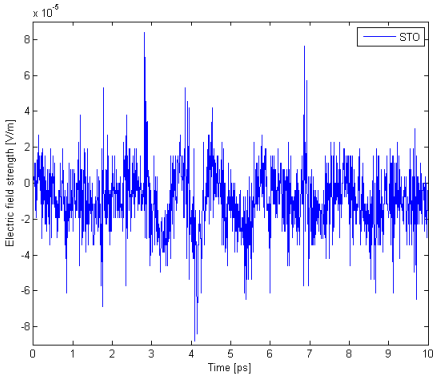

(a) Enlarged region around 4ps time delay

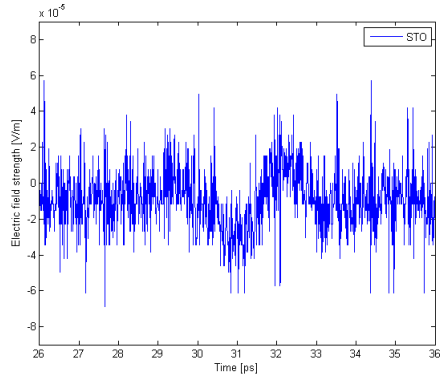

(b) Enlarged section around 30os time delay

Figure 4.6: A more detailed view on the interesting areas

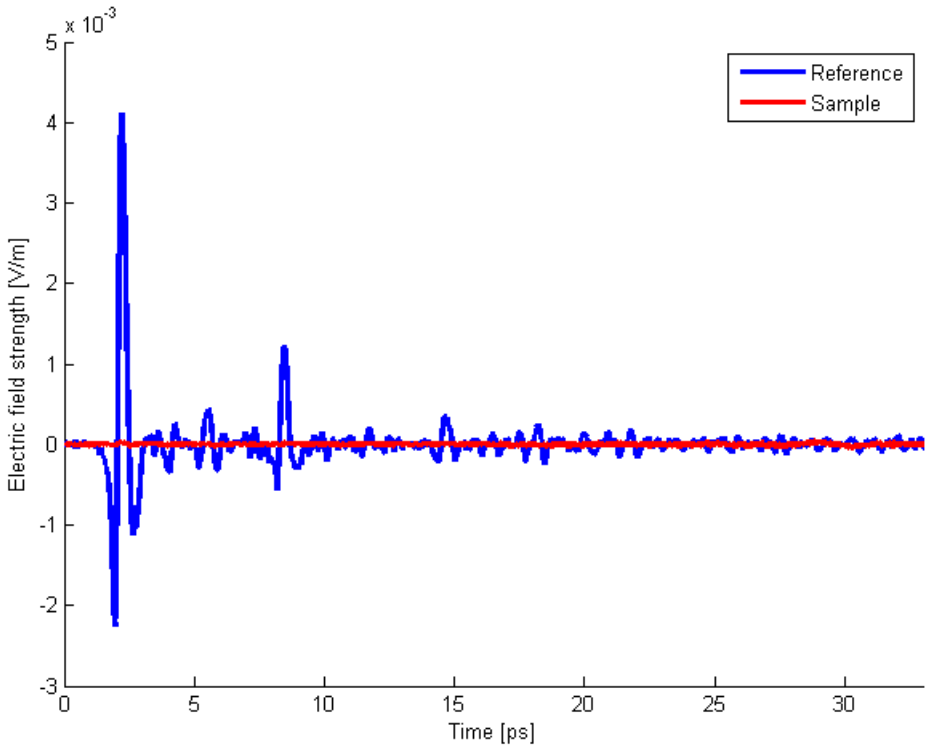

Figure 4.7: THz-TDS signal of $SrTiO_3$ with air as reference

Compared with the air reference, the THz-pulse transmitted through the STO substrate is significantly weaker, making it challenging to distinguish the interesting regions when comparing the two at a normal scale as seen in figure 4.7. A magnified plot of the two regions can be seen in figure 4.8. At the first peak, one can see that the peak seems to overlap with the main peak of the reference signal. The broader peak measured for STO at around 30 ps does not seem to have any similarity to the reference pulse.

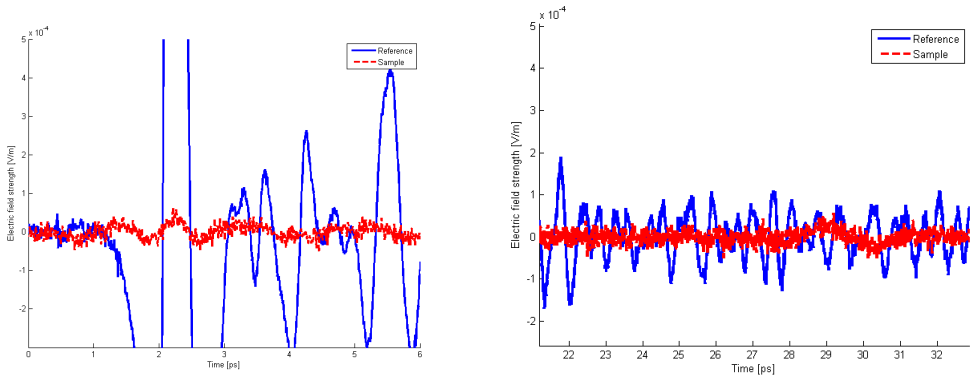

(a) Region around 4ps time delay compared with detected signal for the air reference

(b) Region around 30ps time delay compared with measured air reference

Figure 4.8: Magnified plot for the regions around 4ps and 30ps for STO substrate

Positioning of the first STO peak suggests that either the THz-pulse propagating through the sample see a refractive index in the range of 1, or that some of the beam is not hitting the sample properly.

As can be seen in the discussion section, the criteria for having a valid spectrum α_{max} is not fulfilled for the THz-TDS measurements of *STO prepped*, and has therefore not been plotted. As was mentioned by Jepsen [49] the criteria for the refractive index calculations is not bound by the same α_{max}, the corresponding plots for the two regions at 4ps and 30ps can be seen below. Figure 4.8d shows some interesting behaviour, the measured signal at 30ps relative delay shows a calculated refractive index in the range of 16-19, which is similar to the measurements reported for THz-TDS by Han et al [46] for ¡100¿ single crystal STO having n $\sim$ 19, as well as Katayama et al [53]. The periodic spikes in figure 4.8 is believed to be artefacts caused by inaccuracy for calculation of the theoretical transfer function H_{theory} as will be shown in the discussion section. The first peak measured around 4ps time delay shows a behaviour worth further investigation. Since a measured signal in this region would imply a refractive index $n \sim 1$, it would be a logical assumption to believe it to be caused by some part of the pulse not hitting the sample. However, as the retrieved signal does not have the same pulse-shape as the reference pulse, either does it have a refractive index constant at n=1, it would imply that it does interact with the sample in

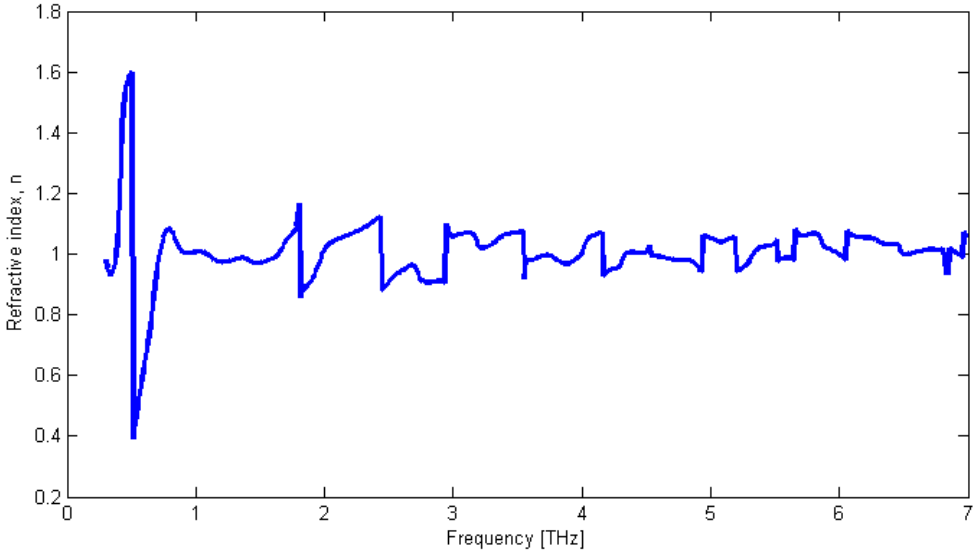

(c) Calculated refractive index for region around 4ps delay

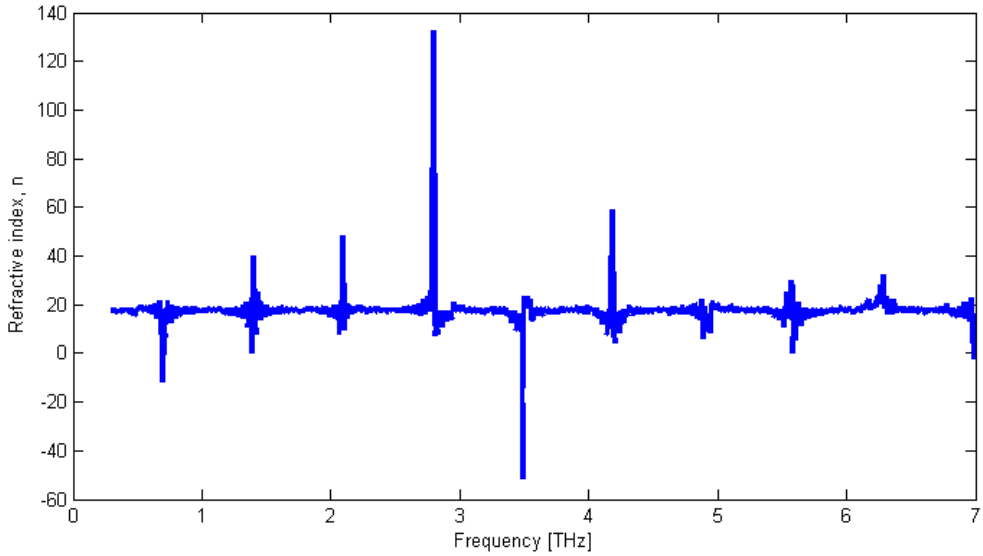

(d) Calculated refractive index for region around 30ps delay

Figure 4.8: Calculated refractive index for $SrTiO_3$ the two regions of interest

some manner. The oscillation around 0.5 THz corresponding to $16.7cm^{-1}$ shows behaviour one would typically expect from a phonon-mode. A similar peak can additionally be found at 1.8 THz, corresponding to $60cm^{-1}$. However, based on

the observed Raman-active phonon-modes in bulk STO having been reported in the region of $90cm^{-1}$ for the TO_1 mode, in addition to the $TO_2 - LO_1$ at $\sim 170cm^{-1}$ [46] makes this a less likely explanation.

4.6 Experimental Results: $BaTiO_3$

Due to the substrate measurements of *STO prepped* indicating low transmittance in the THz-region, it follows that any detected signal for *BTO 100* would show the same limitations in regards to extraction of valuable material parameters.

$$H_{experiment}(\omega) = \frac{E_{\text{BTO on STO}}(\omega)}{E_{STO}(\omega)} \tag{4.14}$$

A long-range plot of *BTO 100* and *STO prepped* can be seen in figure 4.9, with the magnified regions of interest shown in figure 4.10.

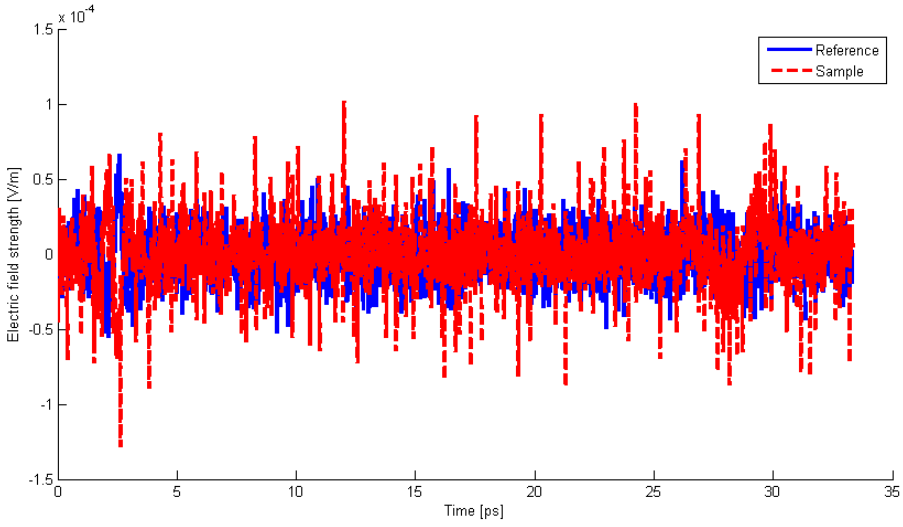

Figure 4.9: THz-TDS measurement of 100nm BTO with STO as reference

These plots suggests that BTO has a refractive index less than one as the sample signal seems to arrive before the reference, the post-processing algorithm was controlled to make sure the reason was not due to any user error. Studies of 22nm and 44nm BTO thin films on MgO substrate done by Misra et al [14] found a refractive index in the range of $12 > n > 6$ for 0.2-2.5THz, for bulk BTO at 1THz they reported n=19. For a BTO thin-film such as the one used in fig.4.9 having thickness of 100nm, a visible time-delay between the BTO and STO prepped measurements would not be expected, as the film would cause Fabry-Perot reflections and interfere with the main-peak itself. This can easily be shown using a lowest estimate for $n_{BTO} = 6$ and thickness of 100nm $\implies \Delta t = 2fs$.

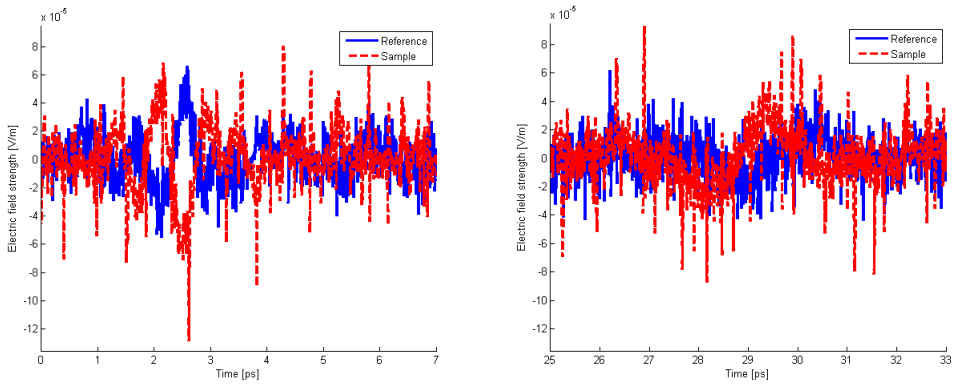

(a) 100nm BTO plotted against STO substrate, region around 4ps

(b) 100nm BTO plotted against STO substrate, region around 30ps

Figure 4.10: THz-TDS measurement of 100nm BTO plotted against STO substrate

Chapter 5

Discussion

5.1 Optical Kerr-effect Spectroscopy

5.1.1 Sample Preparation

The initial trial run of measurements were done on mono-crystalline <111> oriented $SrTiO_3$, prior to any chemical steps or annealing similar to *STO manual*. These samples had one smooth side which was required for later deposition of BTO, and one non-polished side with some inherent surface roughness. When the OKE set-up had been properly aligned a trial run of these STO sample was performed. It was found by visual inspection using the IR sensor card that the incoming $\lambda = 800nm$ probe beam did not reach the detector, and even if the probe and pump power were increased a significant amount of noise hindered any good measurements. The corresponding signal is shown below in figure 5.2a. As shown in figure 5.1a instead of passing through the sample, possibly with some attenuation, the beam instead showed a halo shaped broadening, making it impossible to obtain a reasonable OKE transient signal. A 100nm epitaxial BTO layer on STO was also tried in OKE, with same substrate material, but having undergone various deposition steps, but the findings were similar with pure STO. Different possibilities were examined; absorption was considered, but a literature study found that prior measurements for STO in the $\lambda = 800nm$ range showed very high transmission [44]. The possibility of some other material property causing scattering behaviour was considered, but found not likely. The resulting hypothesis was that the inherent surface roughness on the backside of the STO substrate was the primary cause of this scattering, therefore a procedure for polishing STO was developed.

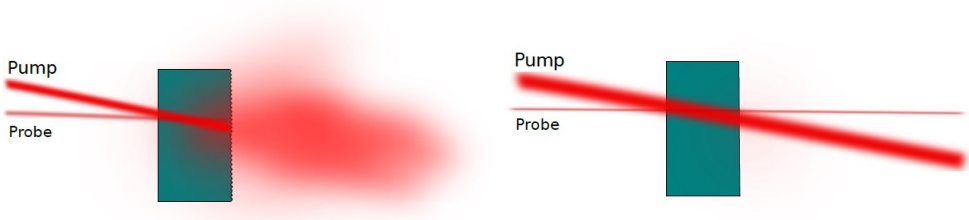

(a) $SrTiO_3$ polished front side, unpolished back (b) $SrTiO_3$ polished both sides

Figure 5.1: $SrTiO_3$ polished front side, unpolished back

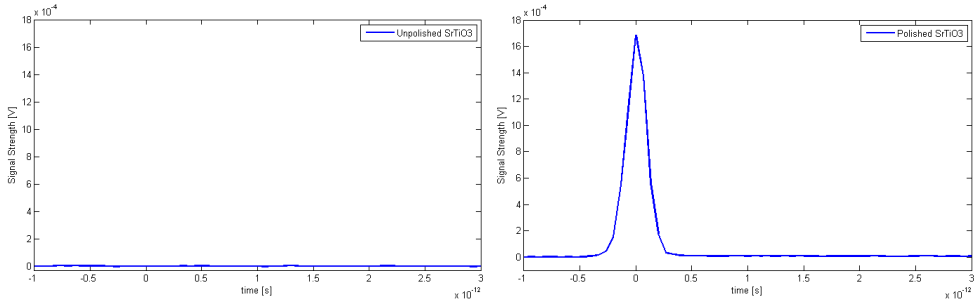

(a) Unpolished $SrTiO_3$ (b) Polished $SrTiO_3$

Figure 5.2: Effect of surface roughness on OKE measurements of $SrTiO_3$

When developing the polishing procedure different paper roughness were used, continuously examining effects on surface structure by visual inspection of the light reflection and by using an optical microscope. After some testing it was found that when using very fine paper only the upper parts of the peaks were removed, and deeper valleys still remained. On the other hand if too rough paper was used, it posed a risk of causing even deeper fractures on the surface, possibly due to either contaminants in the polishing process or due to material properties. In studies it has been shown that STO is a brittle material exhibiting conchoidal fracturing due to the lack of cleavage planes [54]. The resulting method which produced decent results used first a medium roughness paper with relatively light pressure, removing the taller peaks, moving straight to a very fine paper with heavy pressure, making the surface smooth. As this was done by hand it is a source of error due to some slight variation in thickness and surface structure.

This polishing study showed proof of concept, and for even more accurate results it was decided to order a couple of <111> $SrTiO_3$ substrate industrially polished on both sides.

5.1.2 Acetone Measurements

The effect of subtracting the slowly relaxing contribution coming from molecular reorientation for acetone can be seen in figure 5.3.

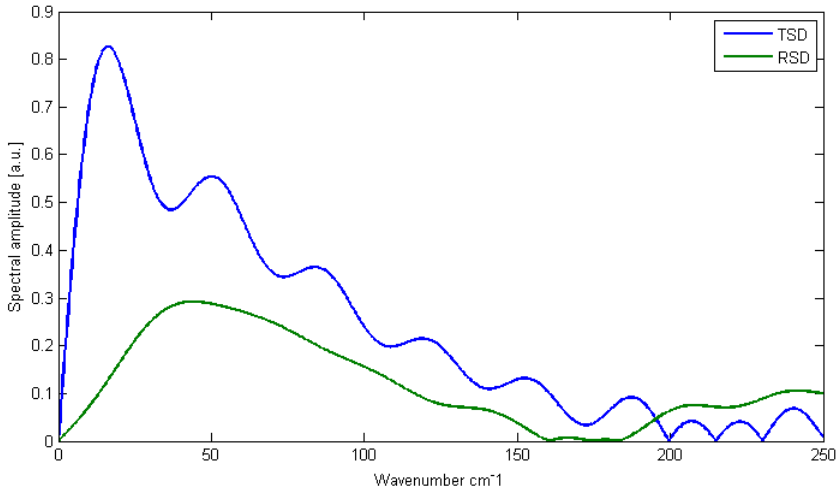

Figure 5.3: Comparison between resulting Raman spectrum with and without long-term relaxation removed

5.1.3 $SrTiO_3$ analysis of time-domain signal

The OKE set-up was aligned and tested by using a variety of water and acetone samples, this step is crucial since measurements depend on having a good overlap of the pump and probe inside the sample. After achieving proper alignment the resulting dynamic range for the various measurements were typically in the range $DR \sim 2000 - 5000$.

Directionality of crystalline lattice

For <111> oriented samples the observed direction of the crystalline axes for an incoming wave can be illustrated as shown in figure 5.4. When compared with figure 2.12 the vector describing the [111] would be be in the z-direction. The [100], [010] and [001] would correspond to the $\mathbf{a}_1, \mathbf{a}_2$ and $\mathbf{a}_3$ directions respectively, and their projections onto the (111) plane is illustrated in figure 5.4. An incoming wave would ideally propagate in the z-direction, where the xy directions in the figure are inserted for readability.

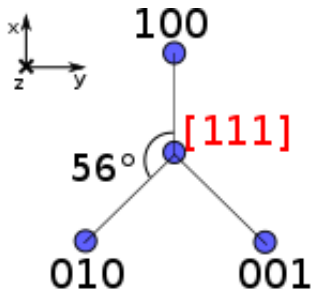

Figure 5.4: Relative angles for the crystalline orientations for STO and BTO cubic and tetragonal symmetry

Observation of a 2nd and 3rd peak

For *STO prepped* and *STO chamber*, as can be seen in figure 3.10b, a visible second peak can be clearly observed at a delay of 7.8 ps relative to the main peak. A possible explanation could be that it is due to a reflection of the pump pulse at the STO-air interface. By using the sample thickness $d_{\text{sample}} = 500\mu$m and refractive index of STO $n(\lambda = 800nm) = 2.3422$ [43] it can be seen that the time delay corresponds well with the expected position of a peak caused by reflection:

$$t = \frac{2 \cdot d_{\text{sample}} \cdot n_{STO}}{c_0} = 7.8ps$$

where $c_0 = 3 \cdot 10^8$ is the speed of light in vaccuum. For *STO manual* on the other hand, the second peak arrives at a later delay, possibly due to either different thickness, or some change in material properties as it has not undergone the same annealing and chemical steps as the two other STO samples. Another interesting observation is the peak around 10ps. It can also be seen that even if the second peak for *STO manual* arrives at a different delay compared to the two others, the third peak still overlap with *STO chamber* and *STO prepped*, making this an observation worth future study.

Plateau between the 1st and 2nd peak

As can be seen in figure 3.10, in the region between the 1st and 2nd peak the measured signal does not relax to zero, which could be attributed to a couple of reasons. At first it would seem that a very slowly relaxing contribution is causing this effect, but this would not explain the sudden drop to zero after reaching the second peak. A hypothesis could be that as the reflected part of the pump overlaps with the probe inside the sample on its way back thereby contributing to the measured OKE signal. That at each delay the reflected pump would overlap with the probe in another part of the material, until they overlap at 7.8 ps again travelling in the same direction in the sample. The sudden decrease could be due to only negligible amount of pump intensity being reflected a second time. There

is one downfall of this hypothesis, mainly that the interaction time where these two pulses overlap would be extremely short, as it would only be in passing, making it questionable if it would be long enough to make an impact on the measured OKE transient. From figure 5.5 it appears that *STO prepped* seems to have slightly slower time constant. To reach a qualitative understanding of the occurring phenomena causing this very slowly decaying intermediate region between the main and second peak further study is required.

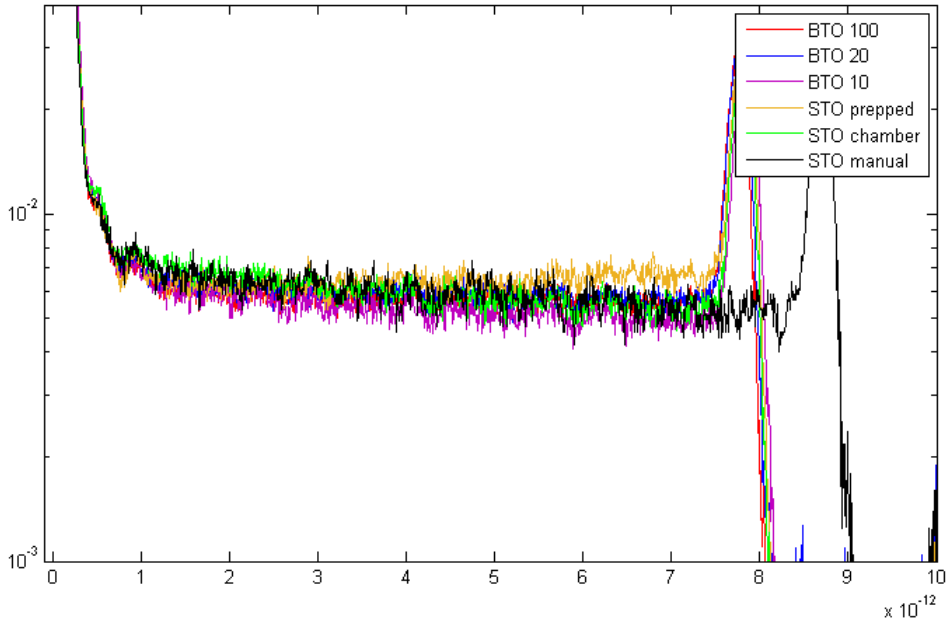

Figure 5.5: Comparison between STO substrate and BTO

5.1.4 $SrTiO_3$ obtained Raman spectrum

In figure 5.6 the normalized total spectral density is plotted for the three STO substrates. The lack of subtraction causes a slight ripple in the retrieved spectrum, the maximum peak position however is similar.

Rotation around optical axis

An interesting observation was seen in figure 3.13, that the relative peak amplitude for *STO prepped* appears to be angle-dependent. A couple of reasons could result in this behaviour, one of them being experimental inaccuracies most likely caused by the beam not hitting exactly at the same sample spot during rotation. Given a non-perfect sample, contaminants such as silver glue from

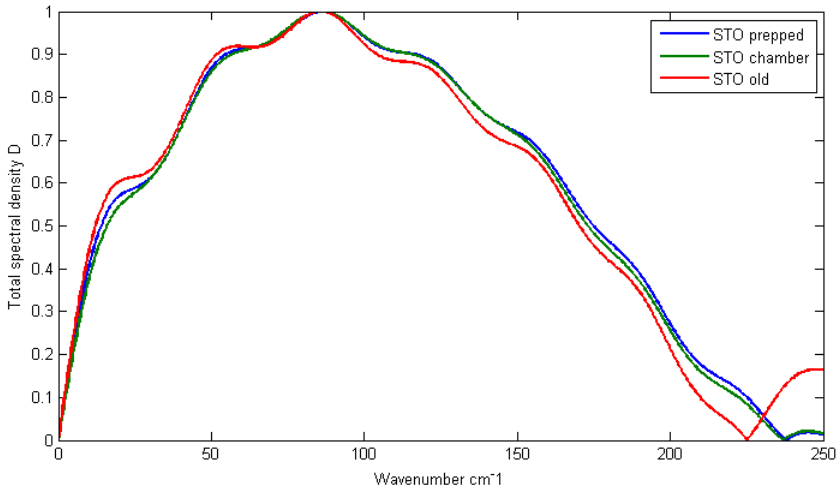

Figure 5.6: Normalized Raman spectrum STO, without slowly relaxing contribution removed

deposition chamber, residual material from chemical preparation or inherent sample inhomogeneity could be the contributing factor for what appears to be angle dependence. Assuming the measured value gives an accurate picture of STO characteristics it suggests a directional dependent third-order susceptibility $\chi^{(3)}$. When comparing with a previously obtained measurement, a similar behaviour can be observed, seen in figure 5.7, suggesting this could be a viable explanation.

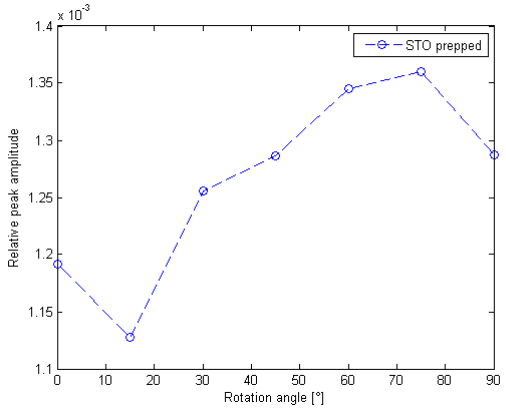

Figure 5.7: OKE angle measurements of STO with slight adjustments in the experimental set-up

General remarks on the validity of the BTO thin-film measurements

A considerable amount of effort went into investigating how the various parameters affected the resulting Raman spectrum for the OKE measurements of BTO. Since it was found that the spectral information was highly dependent on chosen regions this adds considerable uncertainty to the retrieved Raman spectrum. The results shows promise in finding spectral contributions lying in the range of expected quasi-mode frequencies, but these should be confirmed by further studies, to validate that these peaks are not attributed to some other physical effect or post-processing artefact. As the OKE is relying on third-order nonlinear effects it does not enable a straight-forward extraction of these phonon-modes. Considerations such as similar k-vectors between measurements (in regards to sample directionality), similarity in material properties of reference and sample substrate, as well as relative peak displacement between measurements could all possibly contribute to errors in Raman spectrum calculations.

Effect of relative peak positions for the BTO and STO measurements

Since the sample and reference can not be measured simultaneously some slight adjustment of the relative peak-positions have been implemented by some studies [37]. The effect of this shift can be seen in figure 5.9 for *STO chamber*, shifting the relative peak positions by a temporal displacement $-30fs < \tau < 30fs$.

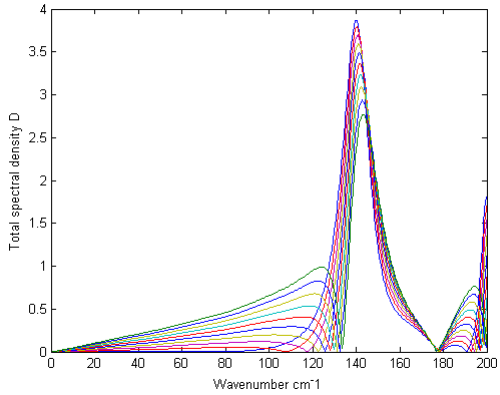

(a) Relative shift of peak position from t=0 to t=-30fs

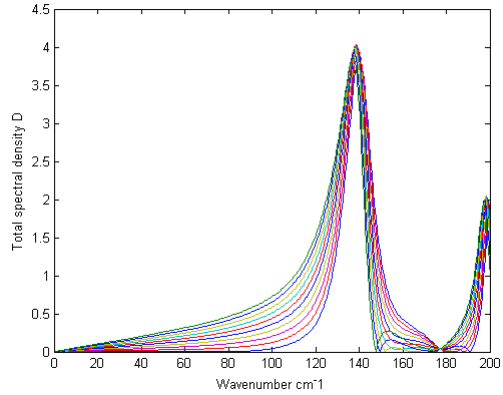

(b) Relative shift of peak position, from t=0 to t=30fs

Figure 5.8: Relative displacement between the measured signals around t = 0 for *BTO 100*

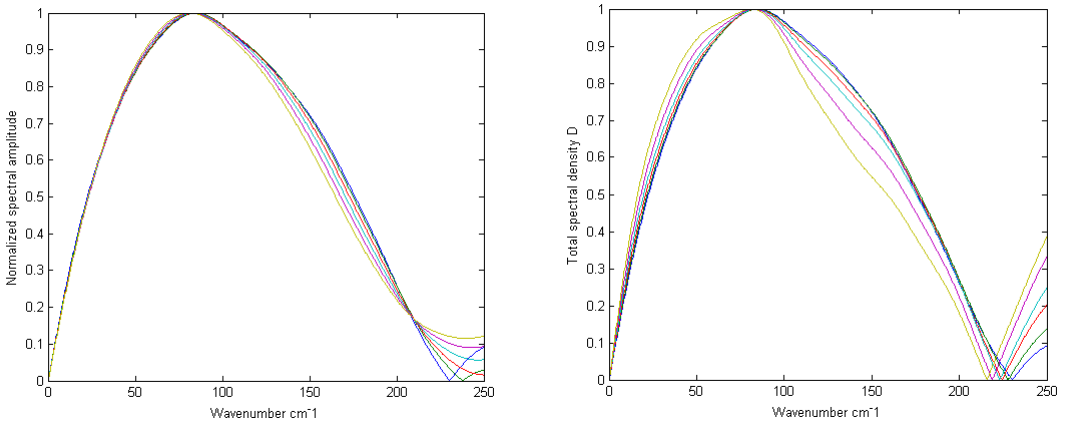

(a) Relative shift i peak position from t=0 to t=-30fs (b) Relative shift i peak position, from t=0 to t=30fs

Figure 5.9: Effect of relative shift on resulting Raman spectrum for *STO chamber*

5.2 Terahertz time-domain Spectroscopy

5.2.1 Sample Preparation

Since the terahertz wavelengths are spatially broad compared to typical inherent surface roughness in the μm range, having unpolished samples are assumed not to cause any significant effect on THz-TDS measurements as discussed in the earlier chapters. However, it is difficult to make any qualitative observations that either confirms or disprove this insensitivity to inherent surface roughness as the THz-TDS measurements as shown in section 4.5 are weak and a subject of considerable uncertainty. A concern when using two separate samples to extract material information such as in OKE and THz-TDS, is that the STO for both samples should show similar material properties. There are various factors that could make for a difference, especially annealing and chemical processing-steps are considered important. Another factor could be local variations in the samples, or variations among samples coming from the same batch. One method to limit some of these uncertainties would be to use one substrate material and deposit BTO on half, while leaving the other half untouched for use as a reference. Thought possibilities however are not always feasible, in this case due to the PLD deposition process making sharply defined edges of the films challenging. It was therefore decided to use one of the 10x10x0.5 mm <111> STO substrates and divide it into four smaller samples, where three of these have been used in the prior experiments namely the *BTO 20*, *BTO 10* and *BTO chamber*.

5.2.2 $SrTiO_3$ and $BaTiO_3$ Measurements

The THZ-TDS measurements on STO showed limited applicability, since even determining position of the detected pulse was not trivial. Similar studies using THz-TDS to investigate $SrTiO_3$ and $BaTiO_3$ have been done by various group, but none have reported using STO as a substrate for BTO measurements. BTO thin-films on MgO substrate by Misra et al. [14], BTO powder form by Wan et al. [55] and STO thin-films measured in THz-TDS reflection mode by Katayama et al. [53] all show the promise of using THz-TDS for perovskite measurements. Sufficiently strong THz-TDS transmission measurement of bulk STO single crystals enabling feature extraction are rarely reported [1].
To investigate if the lack of measured signal could be caused by other effects than absorption and reflection a variety of different possibilities were investigated as will now be discussed.

Positioning of sample along the optical axis

One of the uncertainties is whether the THz-beam hits the sample correctly. Since it has a Gaussian shape and a beam waist of 1 mm, a reasonable assumption would be that as long as the sample is in the Rayleigh range then the sample size should not be an issue. The effect of vertical and horizontal movement of the sample were also investigated without observing any significant improvement. Since the path of THz pulses is not traceable it is assumed the pulse follows to some degree the $\lambda = 800nm$ and the SHG $\lambda = 400nm$ beams, and thus these are used when adjusting the placement of the sample. This assumption was seen to give a reasonable sample positioning when doing THz-TDS on various liquids. As is shown in figure 5.10, three different scenarios should be considered. In position one the sample size is too small in comparison to the beam waist, thus part of the THz-beam is not hitting. In the second position on the other hand, the sample is positioned in the focal plane or Rayleigh range making the whole beam interacting with the sample. At position three however, only a part of the beam is hitting the sample. A thorough investigation of the positioning along the

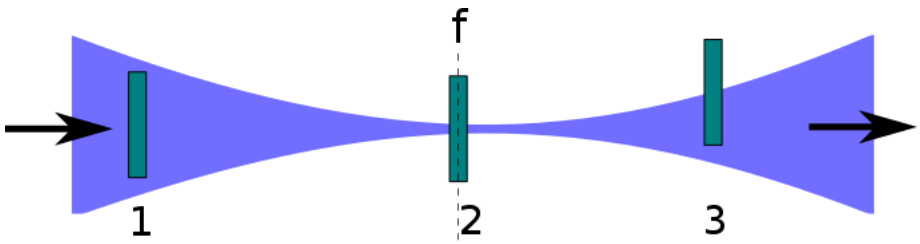

Figure 5.10: Positioning of the sample, three different varieties

[1] Han et al. [46] reported absorption coefficient as well as refractive index for $500\mu m$ thick STO the region 0.1-1 THz, indicating feasibility, but the paper lack any reported time-domain signal

optical axis was performed, but no apparent solution was found. Even when using the *STO prepped* having physical dimensions 10x10x0.5 mm some observed peak around zero delay compared to air-reference could be seen. When moving the sample a sufficient distance away from the assumed Rayleigh-range it could be seen from the measurements that parts of the pulse were no longer hitting.

Possible refraction of THz beam

Since the exact direction of the beam is unknown it is likely that the beam might have some angle and not be at normal incidence compared to the surface. This angle could cause a refraction of the beam, resulting in a displacement of the beam in comparison with the original path. Especially for materials exhibiting high refractive index even smaller angles would cause a measurable displacement as the refraction angle follows Snells law: $n_1 \sin\theta_1 = n_2 \sin\theta_2$. Such a refraction would cause the beam to slightly shift direction at the first interface causing the transmitted beam to have some spatial shift compared to its unaltered path as shown in figure 5.11a. The same effect could be caused by inhomogeneity in the material as illustrated in figure 5.11b. One possibility would be that this shift could cause the wave to travel a slightly different path than it would otherwise (possibly even shorter?). This could be a possible explanation for what is occurring between the BTO and STO shown in section 4.6. One other effect of such a spatial displacement might be that if this shift is large enough the THz and probe pulse would no longer properly overlap in the EO-crystal, thereby making the detection process of the peak the limiting factor and not the interaction of the THz-pulse with the sample. A significant amount of time was therefore spent on testing this hypothesis, changing rotations and measuring changes, but no configuration was found to substantially improve the signal for any of the *STO prepped* or *BTO 100*.

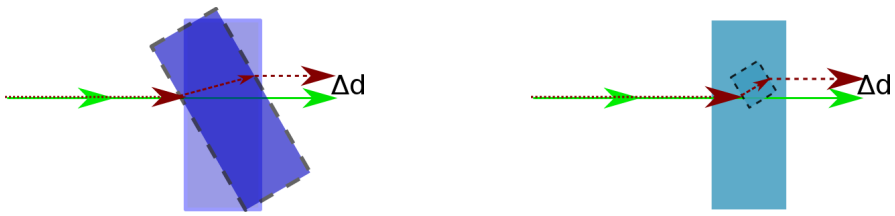

(a) Effect of angle on measurements

(b) Refraction due to inhomogeneity in the sample

Figure 5.11: Possible reasons for refraction in the THz-TDS

Polarization rotation due to anisotropy:

A last considered possibility is that the material could exhibit some anisotropic behaviour, thus causing a shift in the polarization of the THz-beam as it propagates through the sample. The the GaP-crystal is optimized for a certain

polarization for detection of the THz-pulse. This would cause such a shift undesirable as it would make the induced birefringence in the crystal align more along a less desirable direction, thereby causing less polarization shift in the probe and thereby also reducing the detected signal amplitude. This hypothesis was tested by rotating the sample to see how it affected the measurements. Due to the crystalline structure of STO being cubic centro-symmetric the presence of such an anisotropy is found unlikely.

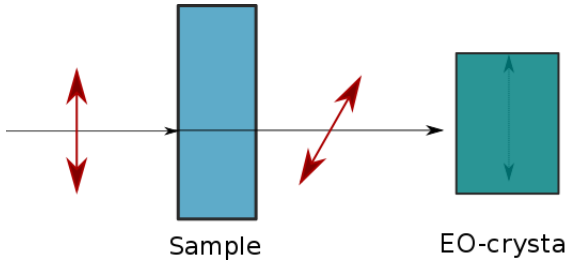

Figure 5.12: Polarization shift due to possible birefringence

5.2.3 Experimental Results:

Validity of measurement:

As transmission measurements using THz-TDS proved to be challenging for STO and BTO, the uncertainty of retrievable experimental parameters is therefore of great importance. In figure 5.13 the corresponding α_{max} for STO is plotted, it can be seen that the validity criterion for the measurements are not fulfilled, which means that no reliable spectral information can be obtained.

Refractive index:

The retrieved refractive index from the STO prepped showed some unexpected behaviour. For the peak arriving at 30ps, found in section 4.5, the baseline approximately lies in the region of expected values, but the large oscillations or spikes does not seem to overlap with any known phonon-modes or absorption bands. It was found that these most likely are artefacts caused by the refractive index calculations. The reason for these sudden spikes which can be seen around 0.7, 1.4, 2.01 and 2.71 THz seems to be attributed to inaccuracies in the numerically optimized transfer function H_{theory}. This can be seen when comparing the respective spike positions in refractive index to corresponding frequencies for the theoretical transfer function. In the region of each spike a deviation between the numerical H_{theory} and measured $H_{experiment}$ can be found. When considering the first peak found at 4ps, the numerical transfer function is found to give a good representation of $H_{experiment}$ as can be seen in figure 5.15. To determine if this signal has any physical value further studies would be required.

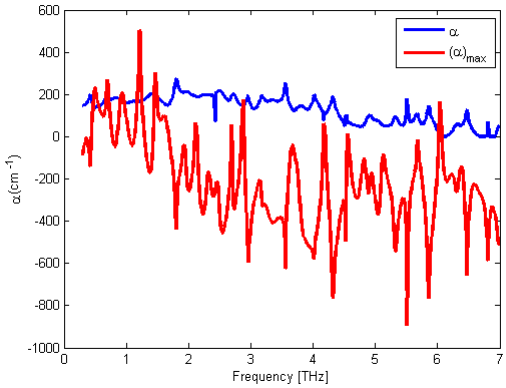

(a) α_{max} for $SrTiO_3$ at position 4ps

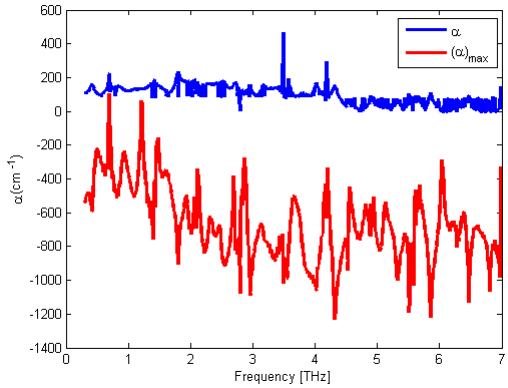

(b) α_{max} for $SrTiO_3$ at position 30ps

Figure 5.13: Calculated α_{max} for THz-TDS of *STO prepped*

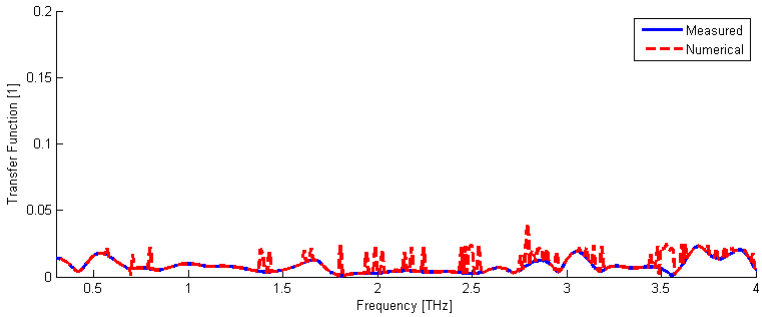

Figure 5.14: Optimized theoretical transfer function for THz-TDS of $SrTiO_3$ for peak around 30ps delay

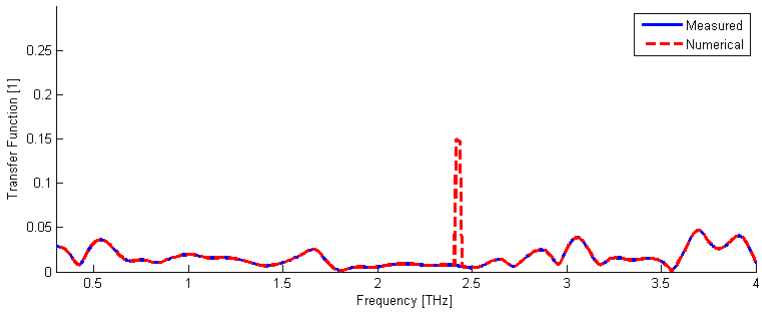

Figure 5.15: Optimized theoretical transfer function for THz-TDS of $SrTiO_3$ for peak around 4ps delay

Chapter 6

Conclusion and future work

The purpose of this masters thesis has been to do ultrafast spectroscopic measurements of $SrTiO_3$ and $BaTiO_3$ with the goal of finding a way to enable measurements of phonon-modes, where especially observations of such modes in the BTO thin-films would be of great interest. It has been shown that transmission measurements using terahertz time-domain spectroscopy yields limited amount of usable information for these particular samples, due to low transmission of terahertz waves for the STO substrate material. A range of plausible causes for this limited transmission has been investigated, suggesting that it is primarily due to high absorption or reflection, where absorption would greatly affect transmission due to the substrate thickness being $500\mu m$. These observations suggests that using an STO substrate for measurements of BTO thin-films in THz-TDS transmission mode is not recommended. As THz-TDS in general serves as a valuable tool for determining absorption bands thereby also phonon-modes, further research would be of great interest and scientific value. To enable these measurements a variety of strategies could be tested, such as using a thinner substrate material, or by using thin-films of $SrTiO_3$ or $BaTiO_3$ deposited on top of a substrate material which shows less absorption in the terahertz regime. A third option which would enable usage of the same samples as the ones which has been used in this study would be to build a THz-TDS set-up for doing measurements in reflection mode.

Alongside the THz-TDS measurements studies have been done using optical Kerr effect spectroscopy. For STO it was discovered that inherent surface roughness on the back-surface caused massive scattering, resulting in the need for samples polished on both sides. The time-domain signals for the resulting $SrTiO_3$ OKE measurements showed some interesting behaviour. After the main peak a slowly relaxing contribution can be seen, which drops to zero after a second peak. As this behaviour does not have any obvious physical explanation, further studies would be of great interest. Future work could be to investigate if the decay-rate and its presence depends on any particular material property or other condition. Such as deposition of a thin-film, out of plane angle, chemical preparation or temperature. Another interesting observation is the peak arriving at a delay of

around 10 ps. As this is not likely to be attributed to any known reflection, such as the one most likely coming from the STO substrate, its occurrence is intriguing, and it would be interesting to see if this has any physical significance. From these measured time-domain signals the corresponding Raman spectra were calculated. The measurements for acetone using a Gaussian approximation for the intensity autocorrelation $G_0^{(2)}$ yielded results which corresponded well with reported values. By using the same procedure for STO it resulted in a peak at around $85cm^{-1}$ which position indicates that this could be an observation of the transverse-optic TO1 phonon-mode. This shows great promise for the detection of phonon-modes in these types of materials by means of OKE. The rotation study on STO suggests that the third-order susceptibility $\chi^{(3)}_{STO}$ is possibly dependent on the orientation of the sample. Caused by the various possible sources of error this study should be repeated to check its consistency. Further study could be to use a variety of STO samples, to get an average, and possibly also for substrates having udnergone different chemical processing steps and annealing temperatures. A more thorough study of the third-order susceptibility for STO would also be a venue worth exploring, as well as estimation of the $\chi^{(3)}_{BTO}$ and see if this is affected by various film-thickness. Studies of BTO using OKE shows promising results, displaying Raman peaks in the range of expected quasi-modes, which could be observations of a combination of the A_1 and E phonon-mode found in BTO. This encourages further work using OKE to enable exact measurement of phonon-modes in BTO. Spectral variations could be seen depending on data chosen for spectrum-calculations, indicating the need for further investigations on how various parameters affect the spectrum, and to confirm that the achieved Raman spectrum is not attributed to any non-physical explanation.

Bibliography

[1] "The Nobel Prize in Physics 1956", http://www.nobelprize.org/nobel_prizes/physics/laureates/1956/index.html. [Accessed: 12-Jun-2016].

[2] Gordon E. Moore, " "Cramming More Components onto Integrated Circuits," *Electronics,* vol. 38, no.8, pp. 114–117, 1965.

[3] R. R. Tummala, "Moore's Law Meets Its Match", *IEEE Spectrum: Technology, Engineering, and Science News, 01-Jun-2006*, http://spectrum.ieee.org/computing/hardware/moores-law-meets-its-match. [Accessed: 12-Jun-2016].

[4] W. G. Nilsen, and J. G. Skinner, "Raman Spectrum of Strontium Titanate," *The Journal of Chemical Physics,* vol 48, no. 5, pp. 2240-2248, 1968.

[5] W. G. Spitzer, R. C. Miller, D. A. Kleinman, and L. E. Howarth, "Far Infrared Dielectric Dispersion in $BaTiO_3$, $SrTiO_3$, and TiO_2," *Physical Review,* vol. 126, no. 10, pp. 1710-1721, 1962.

[6] A. S. Barker Jr. , and M. Tinkham, "Far-Infrared Ferroelectric Vibration Mode in $SrTiO_3$," *Physical Review,* vol. 125, no.5, pp. 1527-1530, 1962.

[7] G. H. Haertling, "Ferroelectric Ceramics: History and Technology," *Journal of the American Ceramic Society,* vol. 82, no. 4, pp. 797-818, 1999.

[8] N. Setter, D. Damjanovic, L. Eng, G. Fox, S. Gevorgian, S. Hong, A. Kingon, H. Kohlstedt, N. Y. Park, G. B. Stephenson, I. Stolitchnov, A. K. Taganstev, D. V. Taylor, T. Yamada, and S. Streiffer, "Ferroelectric thin-films: Review of materials, properties and applications," *Journal of Applied Physics,* vol. 100, no. 5, p.51606, 2006.

[9] M. Dawber, K. M. Rabe, and J. F. Scott, "Physics of thin-film ferroelectric oxides," *Reviews of Modern Physics,* vol. 77, Issue 4, pp. 1083-1130, 2005.

[10] J. F. Scott, and C. A. Paz de Araujo, "Ferroelectric Memories," *Science*, Vol. 246, no. 4936, pp. 1400-1405, 1989.

[11] A. V. Khvalkovskiy, D. Apalkov, S. Watts, R. Chepulskii, R. S. Beach, A. Ong, X. Tang, A. Driskill-Smith, W. H. Butler, P. B. Visscher, D. Lottis, E. Chen,

V. Niktin, and M. Krounbi, "Basic principles of STT-MRAM cell operation in memory arrays," *Journal of Physics D: Applied Physics,* vol. 46, no. 13, p. 139601, 2013.

[12] N. Ortega, A. Kumar, J. F. Scott, and R. S. Katiyar, "Multifunctional magnetoelectric materials for device applications," *Journal of Physics: Condensed Matter,* vol. 27, no. 50, p. 504002, 2015.

[13] M.D. Fontana, K. Laabidi, B. Jannot, "Quasimodes and a central peak in $BaTiO_3$," *Journal of Physics: Condensed Matter,* vol. 6, no. 42, p. 8923, 1994.

[14] M. Misra, K. Kotani, T. Kiwa, I. Kawayama. H. Murakami, and M. Tonouchi, "THz time domain spectroscopy of pulsed laser deposited $BaTiO_3$ thin films," *Applied Surface Science,* vol. 237, no. 1-4, pp.421-426, 2004.

[15] M. Fox, "Optical Properties of Solids," *2nd ed. Oxford; New York: Oxford University Press,* pp.22-57 & pp. 271-279, 2010.

[16] E. Vauthey, "Introduction to nonlinear optical spectroscopic techniques for investigating ultrafast processes," *Univ. of Geneva*, 2006, `http://www.mitr.p.lodz.pl/evu/lectures/Vauthey.pdf`, [Accessed: 12.Jun-2016].

[17] P. A. Franken and J. F. Ward, "Optical harmonics and nonlinear phenomena", *Reviews of Modern Physics,* vol. 35, no. 1, p. 23, 1963.

[18] F. Palombo, I. A. Heisler, B. Hribar-Lee, and S. R. Meech, "Tuning the Hydrophobic Interaction: Ultrafast Optical Kerr Effect Study of Aqueous Ionene Solutions", *The Journal of Physical Chemistry B*, vol. 119, no. 29, pp. 8900–8908, 2015.

[19] Y.-S. Lee, "Principles of Terahertz Science and Technology," *2009 ed. Springer,* pp. 61-76, 2008.

[20] P. U. Jepsen, D. G. Cooke, and M. Koch, "Terahertz spectroscopy and imaging - Modern techniques and applications", *Laser & Photonics Reviews,* vol. 5, no. 1, pp. 124–166, 2011.

[21] H. Hamster, A. Sullivan, S. Gordon, and R. W. Falcone, "Short-pulse terahertz radiation from high-intensity-laser-produced plasmas", *Physical Review E,* vol. 49, no. 1, p. 671, 1994.

[22] X. Xie, J. Dai, and X.-C. Zhang, "Coherent Control of THz Wave Generation in Ambient Air," *Physical Review Letters,* vol. 96, no. 7, 2006.

[23] D. J. Cook and R. M. Hochstrasser, "Intense terahertz pulses by four-wave rectification in air," *Optics Letters,* vol. 25, pp. 1210-1212, 2000.

[24] M.-K. Chen, J. H. Kim, C.-E. Yang, S. S. Yin, R. Hui, and P. Ruffin, "Terahertz generation in multiple laser-induced air plasmas", *Applied Physics Letters,* vol. 93, no. 23, p. 231102, 2008.

[25] J. Dai, X. Xie, and X.-C. Zhang, "Detection of Broadband Terahertz Waves with a Laser-Induced Plasma in Gases", *Physical Review Letters*, vol. 97, no. 10, 2006.

[26] H. C. B. Skjeie, "Terahertz Time-Domain Spectroscopy," *Master's thesis,* Norwegian University of Science and Technology, 2012

[27] "About Lock-in Amplifiers," *Application Note* #3, `http://thinksrs.com/downloads/PDFs/ApplicationNotes/AboutLIAs.pdf`, [Accessed: 28-Apr-2016].

[28] C. Kittel, "Introduction to Solid State Physics," *8th ed. John Wiley & Sons,* pp.469-470, 2004.

[29] F. El-Mellouhi, E. N. Brothers, M. J. Lucero, I. W. Bulik, and G. E. Scuseria, "Structural phase transitions of the metal oxide perovskites $SrTiO_3$,, $LaAlO_3$, and $LaTiO_3$ studied with a screened hybrid functional" *Physical Review B,* vol. 87, no. 3, 2013.

[30] F. Jona, G. Shirane, "Ferroelectric crystals", *Dover Publications INC.*, New York, 1993.

[31] M. J. Wirth, "Ultrafast spectroscopy", *Analytical Chemistry,* vol. 62, no. 4, p. 270A–277A, 1990.

[32] R. Torre (Ed.), "Time-Resolved Spectroscopy in Complex Liquids: An Experimental Perspective," *Springer,* 2008.

[33] E. W. Castner, Y. J. Chang, Y. C. Chu, and G. E. Walrafen, "The intermolecular dynamics of liquid water", *The Journal of Chemical Physics,* vol. 102, no. 2, pp. 653–659, 1995.

[34] G. Giraud, C. M. Gordon, I. R. Dunkin, and K. Wynne, "The effects of anion and cation substitution on the ultrafast solvent dynamics of ionic liquids: A time-resolved optical Kerr-effect spectroscopic study", *The Journal of Chemical Physics,* vol. 119, no. 1, p. 464, 2003.

[35] E. L. Quitevis and M. Neelakandan, "Femtosecond optical Kerr effect studies of liquid methyl iodide", *The Journal of Physical Chemistry,* vol. 100, no. 24, pp. 10005–10014, 1996.

[36] K. Polok, A. Idrissi, and W. Gadomski, "Low frequency response of methanol/acetone mixtures: Optical Kerr effect and molecular dynamics simulations", *Journal of Molecular Liquids,* vol. 176, pp. 29–32, 2012.

[37] K. Mazur, "Ultrafast Dynamics of Water in Aqueous Solutions Studied Through Ultrafast Optical Kerr Effect," *Phd. Thesis, Univ. of East Anglia*, Norwich, UK, pp. 32-38, 2011

[38] D. McMorrow, W. T. Lotshaw "Intermolecular Dynamics in Acetonitrile Probe with Femtosecond Fourier Transform Raman Spectroscopy," *Journal of Physical Chemistry,* vol. 95, 10395-10406, 1991

[39] D. McMorrow, "Separation of nuclear and electronic contributions to femtosecond four-wave mixing data," *Optics Communications,* vol. 86, pp.236-244, 1991

[40] D. Li, Y. Liu, H. Yang, and S. Qian, "Femtosecond nonlinear optical properties of carbon nanoparticles," *Applied Physics Letters,* vol.81, no. 11, p. 2088, 2002

[41] D. Kong, W. Duan, X. Zhang, C. He, Q. Chang, Y. Wang, Y. Gao, Y. Song, "Ultrafast third-order nonlinear optical properties of $ZnPc(OBu)_6$ (NCS)/DMSO solution," *Optics Letters,* vol. 34, no. 16, pp. 2471-2473, 2009

[42] P. Yuan, Z. Xia, Y. H. Zou, L. Qiu, J. Shen, Y. Shen, H. Xu, "Ultrafast optical Kerr effect of phthalocyanine," *Chemical Physics Letters,* vol. 224, no. 1-2, pp. 101-105, 1994

[43] M. N. Polyanskiy. "Refractive index database," `http://refractiveindex.info` [Accessed: 7-Jun-2016].

[44] J. A. Noland, "Optical Absorption of Single-Crystal Strontium Titanate," *Physical Review,* vol. 94, No. 3, 1954

[45] K. Polok, W. Gadomski, F. Sokolić, L. Zoranić, "Molecular dynamics simulations and femtosecond optical Kerr effect spectroscopy of methanol/acetone mixtures," *Journal of Molecular Liquids,* vol. 159, no. 1, pp. 60-69, 2011.

[46] J. Han, F. Wan, Z. Zhu, and W. Zhang, "Dielectric response of soft mode in ferroelectric $SrTiO_3$," *Applied Physics Letters,* vol. 90, no.3, p.31104, 2007

[47] P.U. Jepsen, U. Møller, and H. Merbold, "Investigation of aqueous alcohol and sugar solutions with reflection terahertz time-domain spectroscopy" *Optics Express,* vol. 15, no. 22, 2007.

[48] M. Schall, M. Walther, P. Uhd-Jepsen, "Fundamental and second-order phonon processes in CdTe and ZnTe," *Physical Review B,* vol. 64, no. 9, 2001.

[49] P. U. Jepsen and B. M. Fischer, "Dynamic range in terahertz time-domain transmission and reflection spectroscopy", *Optics letters,* vol. 30, no. 1, pp. 29–31, 2005.

[50] M. Naftaly, and R. Dudley "Methodologies for determining the dynamic ranges and signal-to-noise ratios of terahertz time-domain spectrometers," *Optics Letters,* vol. 34, no.8, pp. 1213-1215, 2009

[51] T. Sørgård, "Terahertz Time-Domain Spectroscopy of thin material samples," *Master's thesis,* Norwegian University of Science and Technology, 2015

[52] I. Pupeza, R. Wilk, and M. Koch, 'Highly accurate optical material parameter determination with THz time-domain spectroscopy', *Optics express*, vol. 15, no. 7, pp. 4335–4350, 2007.

[53] I. Katayama, H. Shimasato, M. Ashida, I. Kwayama, M. Tonouchi, and T.Itoh, "Observation of Soft-Mode hardening and Broadening in $SrTiO_3$ Thin-films by Broadband Terahertz Time-Domain Spectroscopy," *Quantum Electronics and Laser Science Conference,* QELS '07, pp. 1-2, USA, 2007.

[54] T. Chien, N. P. Guisinger, and J. W. Freeland, "A survey of fractured SrTiO3 surfaces: from the micro-meter to nano-meter scale," *J. Vac. Sci. Technol. B* vol. 28, no. 4, 2010

[55] F. Wan, J. Han, and Z. Zhu, "Dielectric response in ferroelectric BaTiO3", *Physics Letters A,* vol. 372, no. 12, pp. 2137–2140, 2008.

Appendix A

Additional OKE and THz-TDS information

A.1 Physical experimental quantities

A.1.1 Number of photons in one pulse

The output from the fs-laser is measured as around $P_{source} = 3.35W$ at a 1kHz repetition rate. For the 800nm pulse we have the following:

$$E_{pulse} = \frac{3.35W}{1kHz} = 3.35mJ \tag{A.1}$$

We can calculate the approximate number of photons quite easily, as we have $\lambda = 800nm$ corresponding to $\nu = 375$THz:

$$N_{photons} = \frac{E}{h\nu} = \frac{3.35mJ}{h\nu} \approx 1.35 \cdot 10^{16} \tag{A.2}$$

where $h = 6.626 \cdot 10^{-34}$J $\cdot$ s is Planck's constant.
What is calculated above is the number of photons in the pulse coming directly out of the laser. This is divided into the THz and OKE setup, and attenuated by adjustable filters to get the desired excitation power. For a pump with 8mW power the OKE this would give:

$$E_{pump} = \frac{8mW}{1kHz} = 8\mu\text{J} \tag{A.3}$$

$$N_{photons} = \frac{E}{h\nu} = \frac{8\mu J}{h\nu} \approx 3.22 \cdot 10^{13} \tag{A.4}$$

A.1.2 Peak power

Even if a pulse with an energy of 3.35mJ might not seem that much, due to the pulsewidth being in the range of 100 fs this results in a massive P_{peak}. As an

example if one regards the pulse as a soliton (no temporal or spectral broadening) and having a sech^2 shape:

$$P_{peak} \approx 0.88 \cdot \frac{E_{pulse}}{\tau_{pulse}} = 0.88 \cdot \frac{3.35mJ}{100fs} \approx 29.5 \cdot 10^9 \text{W} \tag{A.5}$$

A.1.3 Principle of old OKE setups:

Compared to the set-up shown in figure 3.5 using EO with balanced detection, many previous OKE setups used a set of polarizers and a single sensitive detector instead, as illustrated in figure A.1. It worked by using a linear polarizer being shifted 90°. If no birefringence in the sample was present it would mean that the probe maintained its original polarization and got blocked by the second polarizer, only a polarization shift would allow for a portion of the pulse to be transmitted. One way of obtaining heterodyne detection is by using quarter-wave and half-wave plates as was implemented by Quitevis et al. [35] shown in figure A.2. By first blocking the pump and optimizing the probe to obtain a minimum static signal in the photodiode, and then rotating the polarizer $\leq 1°$ heterodyne detection was achieved.

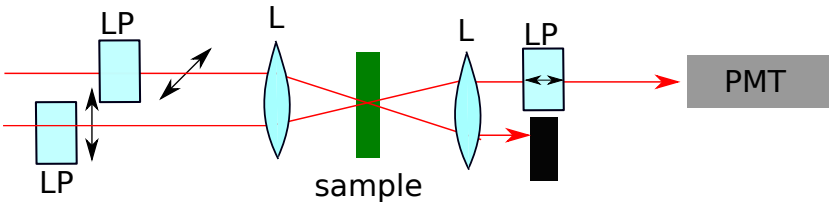

Figure A.1: Schematic for old OKE measurements

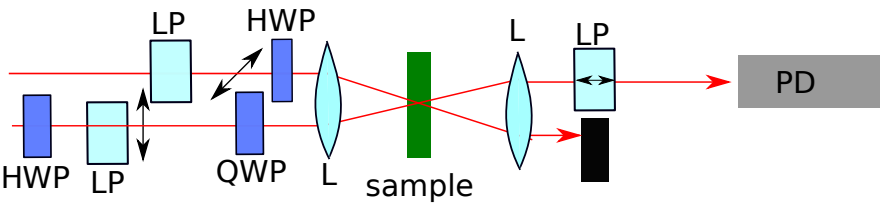

Figure A.2: Schematic experimental OKE setup using linear polarizers with additional HWP and QWP for obtaining heterodyne detection

A.2 Measured Bandwidth loss for the OKE setup

Towards the end of this project a controlling measurement of the spectrum was performed at the OKE side of the optical set-up using a spectrometer measuring the scattered light from an aluminium diffuser. It was found a more reduced spectral content than expected. After a systematic study measuring the transmission through the different optical elements it was found most likely to be caused by a couple of beam-splitters. As stimulated Raman scattering is directly dependent on bandwidth, this adds some uncertainty, but as the pulse is very strong, it is still believed that enough photons in the wide spectral range is transmitted through the set-up to enable reliable OKE measurements.

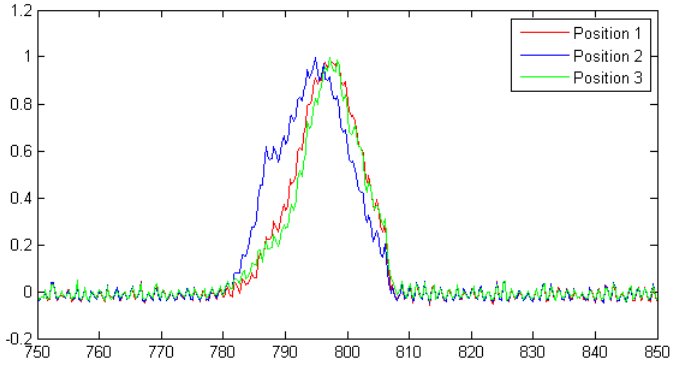

(a) Measured spectrum from an aluminium light diffusor at various positions

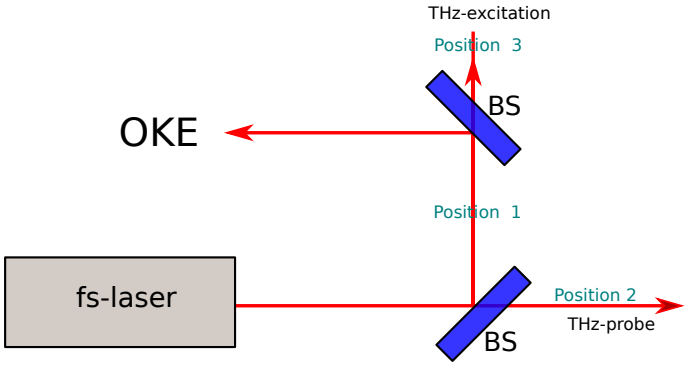

(b) Measured positions

Figure A.2: Spectrometer measurements